NON-LINEAR FRACTURE MECHANICS OF INHOMOGENEOUS QUASI-BRITTLE MATERIALS

V. C. Li
University of Michigan, Ann Arbor, Michigan, USA

ABSTRACT

This chapter presents a survey of non-linear fracture mechanics of inhomogeneous quasi-brittle material. The large scale bridging in the fracture process zone is explicitly modelled as cohesive spring-like tractions and its implications on crack formation and limitations of linear elastic fracture mechanics are discussed. A model of tension-softening is described to illustrate the possibility of relating the micromechanical mechanisms and the material structure to composite non-linear fracture property. Finally, recent research on experimental determination of tension-softening behavior in inhomogeneous quasi-brittle materials is reviewed.

1. INTRODUCTION

A large class of engineering material, including brittle matrix fiber and particulate reinforced composites, single phase polycrystalline ceramics, and rocks, display quasi-brittle behavior as a result of a toughening mechanism known as bridging. Bridging occurs when, for example, fibers crossing a matrix crack in a fibrous composite provide a closing pressure on the crack flanks. Debonding and frictional pulling out of the fibers drains part of the available elastic strain energy release into the crack tip zone, and is reflected as requiring a higher crack driving force. That is, the material appears to be tougher than when no bridging action is present.

In fiber composites, bridging actions have been observed in fiber reinforced mortar [e.g. 1,2], in fiber reinforced thermoplastics [e.g. 3,4] and in whisker reinforced ceramics [e.g. 5,6]. In particulate composites such as ceramics reinforced with ductile particles [e.g. 7], or in concrete -- cement reinforced with aggregates [e.g. 8], the bridging action is contributed by the particles and aggregates which may elastically rupture, plastically yield, or frictionally pulled out. In materials like polycrystalline ceramics and rocks, bridges may be provided by partially broken grains or grain ligaments. Such bridging actions have been observed in alumina, graphite and glass ceramics [9, 10, 11, 12]. In polymers, bridging by crazing at a crack tip [e.g. 13] and bridging in certain rubber toughened polymers under specific conditions have been observed.

The bridging forces, the extent of the bridging zone and the resulting toughening effect can differ significantly from material system to material system. However, it is possible to formulate the fracture problem in such materials in a general way based on the notion of a smeared-out stress versus displacement relationship which could be regarded as a kind of 'cohesive' traction acting across the crack tip process zone. This averaged stress-displacement relationship would include all effects of ligament volume fraction, stiffness, fracture or yield strength, interface bond properties and other relevant factors. Mathematically, it is convenient to think of this cohesive traction as if provided by (possibly non-linear) springs since the cohesive traction generally depends on the displacement across the crack flanks.

The analysis of fracture propagation in the presence of large scale bridging zone is motivated by the need of having an analytic tool for predicting structural behavior, particularly the ultimate strength, when the material fails by fracture advance, and yet the LEFM theory suitable for small scale yielding and elastic plastic fracture theory suitable for ductile material, are inapplicable. This occurs in the quasi-brittle material systems mentioned above, especially when the part size is small in comparison to the bridging zone size. In addition, there is increasing interest in understanding the formation process of a macroscopic crack, and the prediction of the level of toughening that could be achieved by various bridging mechanisms in inhomogeneous composite bodies. In this chapter, we first discuss in Section 2 the modelling of non-linear fracture propagation and the development of the bridging process zone, based on a given relationship between the traction and crack flank opening (the spring law) in the bridging zone. A specific spring law is then developed in Section 3 for fiber reinforced concrete to illustrate the dependence of composite fracture behavior, including R-curve behavior, on the material structure and on micromechanisms of deformation. Finally, in Section 4, experimental techniques for determination of the spring laws of any quasi-brittle material are presented.

2. FRACTURE PROPAGATION AND PROCESS ZONE DEVELOPMENT

In this section, we shall first examine how the spring laws relate to the uniaxial tensile behavior of a material system. The contribution of bridging to toughness will be presented through a generalized spring law description. Subsequently the relationship between a special type of spring law, a tension-softening curve, and the development of the bridging process zone is described. The limitation of the theory of linear elastic fracture mechanics (LEFM), in the presence of a large scale bridging zone will be discussed.

2.1 The Concept of Bridging Forces and its Contributions to Toughening

For convenience, it may be useful to envision a uniaxial tensile response of a brittle matrix composite reinforced with short frictionally bonded fibers aligned in the direction of applied loading. Prior to matrix failure, the composite response may be approximated by a linear elastic stress-strain curve with stiffness given by the law of mixture. After the matrix cracks, the maximum post-cracking stress may or may not be higher than the cracking stress, depending on the fiber volume, fiber aspect ratio and the bond strength (Figure 2.1) Prior to the maximum post-cracking stress, only the fibers along this fracture surface are carrying the load, and elastic debonding at the fiber/matrix interface may occur, if the fibers are strong enough not to rupture. When the maximum post-cracking strength is reached the fibers are fully debonded and slide out with frictional resistance, leading to a softening behavior with continued crack opening.

If the uniaxial specimen is unloaded at the matrix cracking strength, and then reloaded from zero crack opening, the tensile load σ_b versus crack opening displacement δ would give the required spring law (Figure 2.2). It should be noted that the spring law is given by a relationship between stress and displacement, not stress versus strain. This distinction is

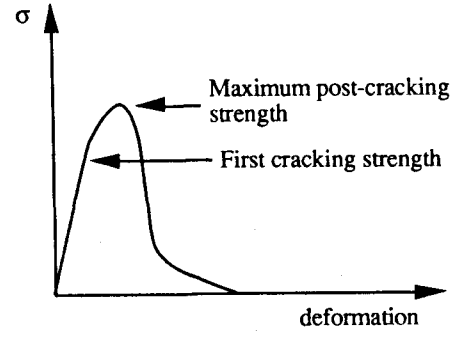

Fig. 2.1: Schematics of a tensile stress-deformation relationship of a composite

made necessary by the fact that in most quasi-brittle material systems, macroscopic scale fracture occurs on essentially a single plane such that classical strain measures would loose their physical meaning.

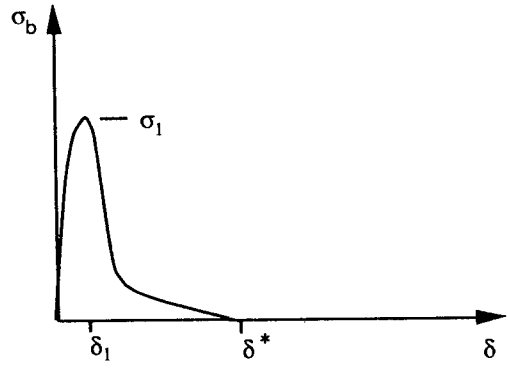

Fig. 2.2: Schematics of a stress-displacement spring law

If we now apply this spring law as a constitutive relationship for the crack tip zone of a structure containing a large steady state crack, the stress as a function of location along the crack line would look something like that shown in Figure 2.3a. The stress ahead of the crack tip can be described by the classical linear elastic crack tip stress field with intensity given by K_m corresponding to the toughness of the matrix. In the process zone, the stress rises with the crack opening following the spring law. At some point in the process zone behind the crack tip, the opening will be large enough such that the softening behavior of the spring will dominate.

In order to consider the approximate effect of bridging on toughening at steady state, (steady state here means that the process zone has reached a fixed size and simply translates as the physical crack extends under increasing applied load), it will be convenient to consider the crack tip region, including the process zone, to be contained in a far field K-dominant region. Following Budiansky [14], Rose [15], and Marshall and Evans [16], applying the J-integral [17] for the closed contour shown in Figure 2.4, the three contributions of the J-integral are:

$$J_\infty + J_b + J_{tip} = 0 \qquad (2.1)$$

The J_∞ term represents the far field applied load and contains information on the structural geometry. The J_{tip} is the critical J value for advancing the crack against the matrix toughness. It is generally more rigorous to describe this 'matrix toughness' as one that

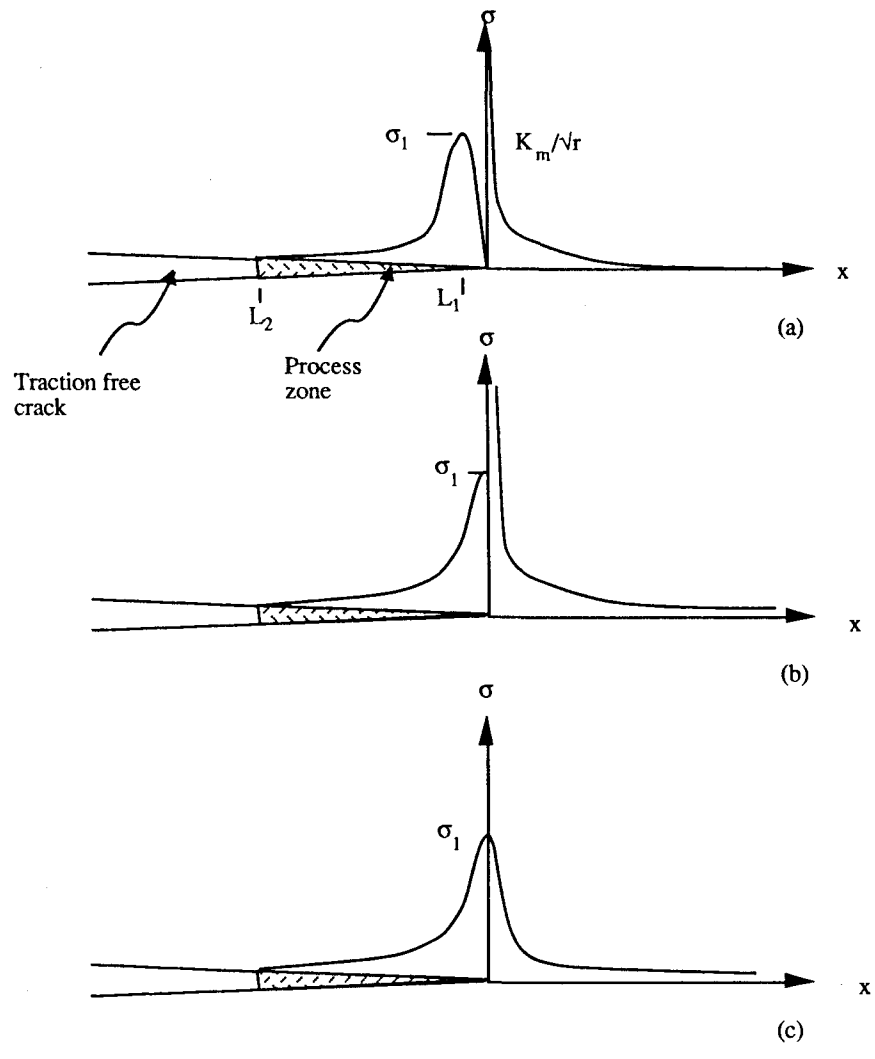

Fig. 2.3: Stress distribution along the crack line for (a) the most general situation, (b) the case when rising part of the spring law is unimportant or lumped as part of the matrix toughness, and (c) the case when the softening part of the spring law dominates the fracture propagation behavior

includes the possibility of non-straight crack front due to bowing around fibers or bridging particles. The mechanics of crack front trapping has been studied by Rose [18] and Rice [19]. Finally J_b is the energy consumed by the extended springs in the process zone. Thus in terms of energetics, (2.1) implies that the energy release rate associated with far field

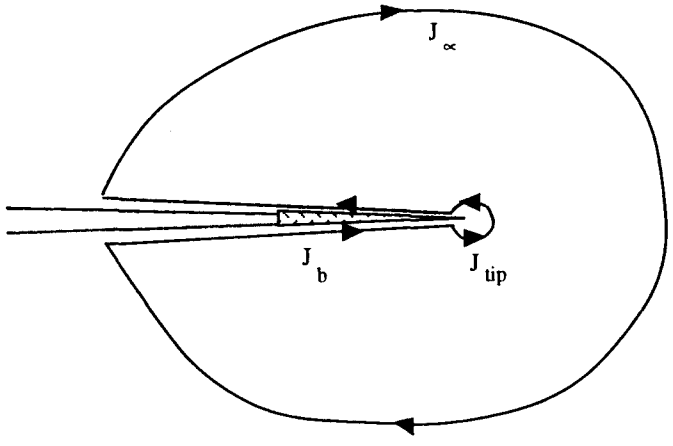

Fig. 2.4: J-integral contour around fracture process zone and crack tip

loading is absorbed by the creation of unit matrix fracture surface, as well as by the spring deforming process. Each of these terms can be written out more explicitly, so that (2.1) becomes

$$\frac{K^2(1-\upsilon^2)}{E} = \frac{K_m^2(1-\upsilon^2)}{E} + \int_0^{\delta^*} \sigma_b(\delta)\, d\delta \qquad (2.2)$$

where K_m is a modified matrix toughness, E and ν are the composite Young's Modulus and the Poisson's ratio, and δ^* is the critical opening at which the spring loses all load carrying capacity. Clearly the integral term in (2.2) is just the area under the spring constitutive law.

Equation (2.2) may be regarded as a generalization of the now familiar fracture criteria of Irwin [20], Barenblatt [21] and Dugdale [22]. Equation (2.2) reduces to Irwin's fracture criterion if the bridging zone does not exists, so that fracture propagation is resisted by the matrix toughness K_m only. If, on the other hand, K_m is negligible compared to the bridging term, as in the case of certain fiber reinforced composites with low toughness matrix, then equation (2.2) reduces to a form similar to the fracture criterion expressed by

Barenblatt. Finally, if again, K_m is negligible, and that σ_b is a constant independent of δ, then Dugdale's fracture criterion will result.

In some material systems, such as those with particle bridges which deform elastically and then fractures (as may be the case for certain particulate reinforced ceramics and high strength concrete), the softening tail part of the $\sigma_b(\delta)$ curve does not exist, and the bridging process zone goes out to L_1 only (Figure 2.3a). The amount of toughening for such a system can be written in terms of a positive spring stiffness (meaning spring force increases with increasing displacement) determined by the volume fraction, fracture strength and elastic stiffness of the particles (see, e.g. [14]). In some cases (probably in normal strength concrete and in alumina), the area under the $\sigma_b(\delta)$ curve up to δ_1 is likely to be small compared to the area up to δ^* so that the energy in opening the springs up to δ_1 could be lumped into an effective K_m, and the process zone contains only a tension-softening part (Figure 2.3b). In materials like short fiber reinforced concrete, the integral term in (2.2) contributed mainly by a softening spring reflecting the large amount of energy absorbed by fiber friction pull-out overwhelms the effective K_m term, and the stress distribution along the crack line will be well approximated by that shown in Figure 2.3c.

In certain engineering systems where crack opening must be restricted, it may be appropriate to neglect the contribution of the softening part of the $\sigma_b(\delta)$ curve to the overall toughness if stringent crack opening limitation is required. In other engineering systems such as in concrete structures, certain amount of crack opening is routinely tolerated, and the part or all of the softening $\sigma_b(\delta)$ curve may be counted to provide composite toughness. In all cases, this softening part of the curve is important to withstand accidental overloads to provide structural integrity.

2.2 Relation Between Tension-Softening And Process Zone Development

We now turn our attention to the case for a composite with a bridging zone in which the cohesive traction is well represented by a softening $\sigma_b(\delta)$ curve, as shown in Figure 2.3b or 2.3c, and when the steady state has not been reached. Other cases where the rising part of the curve is important could be similarly analyzed (see, e.g. [23]). It may be useful to consider the crack as being in the formation process prior to steady state.

For simplicity, consider a crack growing in an elastic body loaded remotely by σ_∞. The governing equation for equilibrium gives the tensile stress on the crack line as:

$$\sigma = \sigma_\infty + \int_{crack} G(x-x')\frac{\partial \delta(x')}{\partial x'} dx' \qquad (2.3)$$

where the integral is to be carried over the crack line. A supplementary equation providing the condition for crack extension is needed and can be written as:

$$K_{\infty} + \int_{bridge} f(c,x')\sigma_b(x')dx' = K_m \qquad (2.4)$$

The influence functions G and f in (2.3) and (2.4) embody information on the structural geometry and the loading configurations. For the numerical illustrations shown below, we have used those corresponding to a crack of total (including the length of the process zone) length c in an infinite body (see, e.g. [24]). In (2.3), the stress σ is identified as the bridging traction σ_b and forms a functional relationship with δ in the process zone. Thus (2.3) and (2.4) form a set of integral equations in δ which in general must be solved numerically. Various simplifications have been made such as by assuming a linear $\sigma_b(x)$ traction distribution in the process zone [25], or by assuming a linear or parabolic shape of the crack face [26] in the solution of these equations. A complete numerical solution of these equations have been obtained by Li and Liang [24] for the case where K_m is small compared to the bridging integral term in (2.4). This assumption is appropriate for certain fiber reinforced composite systems but would not be correct for single phase ceramics, where the K_m term and the bridging contribution to toughness are probably on the same order of magnitude [27]. The non-linear fracture model represented by (2.3) and (2.4) have been employed in various forms by a number of researchers. These include, e.g. Hillerborg et al [28] in concrete, Ingraffea and coworkers in concrete [29] and rock [30], Mai and Lawn [31] in alumina ceramics, and Wnuk and co-workers (see, e.g. references in the chapter by Wnuk in this text) in polymer.

Following [24], the complete solution of (2.3) and (2.4) allows the crack shape profile and the stress distribution profiles to be determined. Figure 2.5 illustrates a quarter of the crack shape profile symmetrical about both axes. The characteristics of this profile is that the crack tip zone closes smoothly as u(x) -> $x^{3/2}$ whereas the classical LEFM crack profile u(x) is quadratic in x. This is the case if the presence of the fracture process zone eliminates the stress singularity at the crack tip.

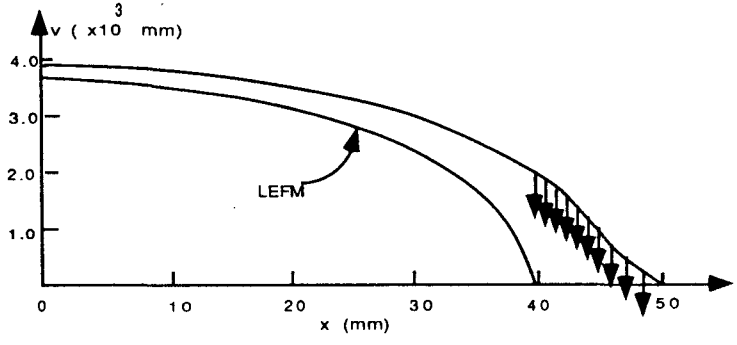

Fig. 2.5: The calculated crack opening profile symmetric about the x and y-axis

The resulting stress profile is shown in Figure 2.6. In approaching the crack tip, the stress rises to the composite tensile strength and decays to zero as the crack opens in the process zone. The LEFM stress profile is also shown for reference. These two curves are expected to overlap should the process zone size l_p reduces to zero. The tension-softening curve used in this calculation is shown in the insert of Figure 2.6.

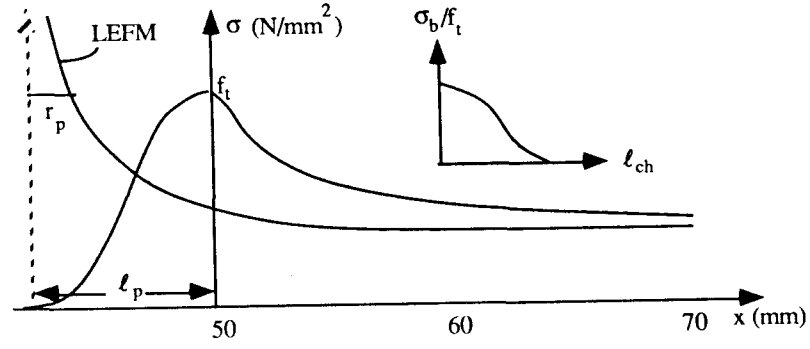

Fig. 2.6: The calculated stress distribution along the crack line

An interesting result of this analysis is the evolution of the process zone (Figure 2.7). The horizontal dashed line represents the critical opening value δ^*. When the opening exceeds this value, the traction is reduced to zero. Four stages of increasing crack opening displacements are schematically shown on the lower half of Figure 2.7. The first two of these stages illustrate the growth of this process zone without growth of the physical crack In the third stage, the physical crack grows with a further extension of the process zone length. In the fourth stage, the physical crack grows further with a small decrease in the process zone length. After this, steady state is reached, whereby the process zone length remains constant and translates to the right as the physical crack grows.

Figure 2.8 schematically illustrates the same process observed by ultrasonics and in-situ microscopy technique in a crack wedged open in a Westerly granite [32]. The light shaded zone denoted as "partially separated with geometrical or frictional resistance to crack opening" can probably be associated with the inelastic processes induced by the K_m singularity or the increasing branch of the σ_b-δ curve and the part of the process zone labelled L_1 in Figure 2.3a. This part is not modelled in the present analysis but could be included as described earlier. The dark shaded zone denoted as "frictional resistance to crack opening" is likely associated with the softening branch of the σ_b-δ curve. The experimental observations illustrated in Figure 2.8 suggest that only after some growth of this process zone does the physical crack begin to extend, just as predicted by the theoretical analysis.

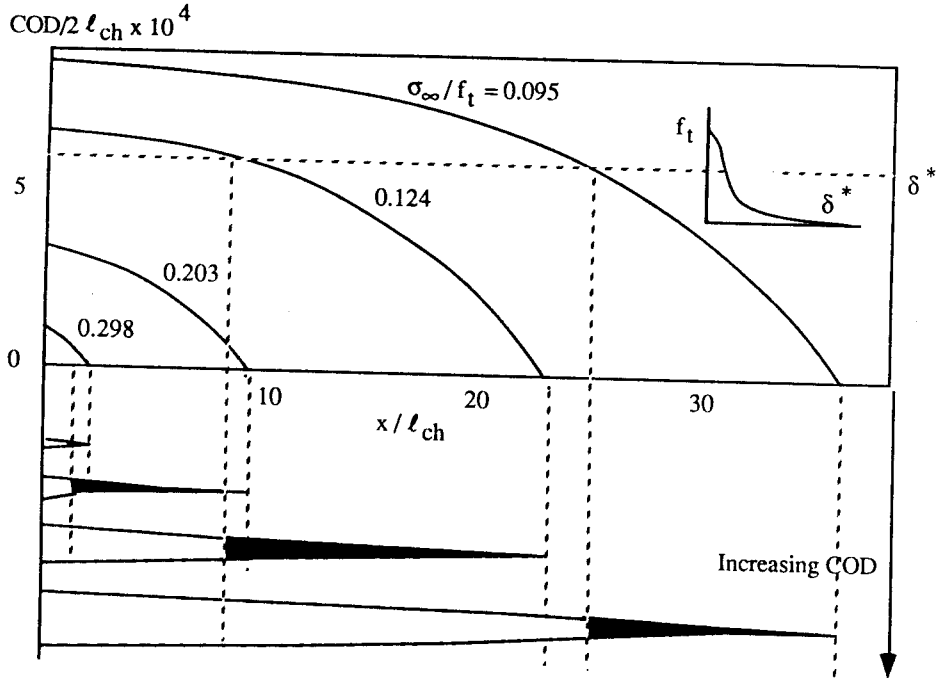

Fig. 2.7: The calculated stages of fracture process zone development

The R-curve of quasi-brittle material, denoting the increasing amount of energy absorbed in the process zone, has been measured by a number of investigators (e.g. [31], [33]) in the form of increasing critical energy release rate or apparent fracture toughness with a certain measure of increase in crack length. It should be clear that in quasi-brittle material, this increased energy absorption is due to the growth of the process zone as described above, and that once the process zone is fully developed, the plateau of the R-curve would be reached. Examples of R-curve calculations are given in section 3.4.

The details of the process zone evolution and translation is obviously related to the shape of the σ_b-δ curve, but less obvious is that they are also influenced by the stress field surrounding the process zone. This implies that with different loading configurations and specimen geometry, it may be expected that the details of the process zone growth observed

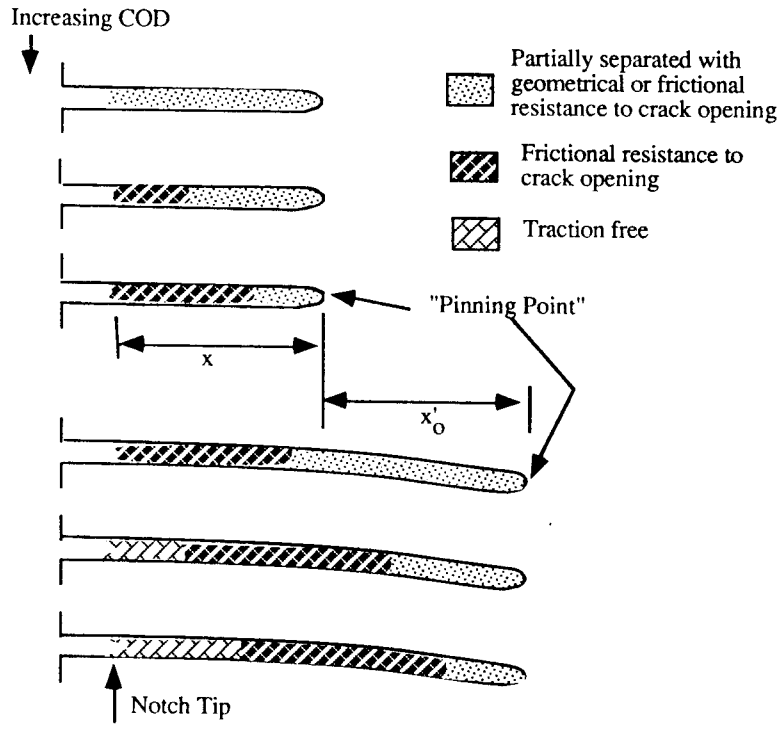

Fig. 2.8: Schematics showing the development of the fracture process zone in Granite by ultrasonic and in-situ microscopy techniques (adapted from [32])

would also be different [24]. Because the R-curve is associated with the process zone development, its shape may be expected to be influenced by these same factors. Hence the R-curve should not be regarded as a material property. As an example, Figure 2.9 illustrates a double cantilevered beam with different loading configurations and the corresponding R-curves. This point is particularly important as the slope of the R-curve in association with the point of specimen instability, is sometimes used to extract information regarded as a material property (e.g. [34]). In some cases where the specimen geometry and loading configuration is such that the crack tip stress field is similar, such as in a three point bend specimen and in a compact tension specimen, the resulting R-curve may look quite similar.

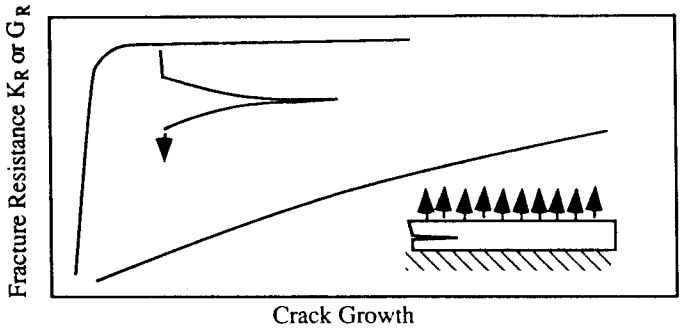

Fig. 2.9: Two different R-curves obtained for the same material from two different specimen geometry and loading configurations

2.3 Limitation of Linear Elastic Fracture Mechanics

For the cracked structure described in the previous section, the ultimate load can be predicted based on LEFM theory. When plotted against a normalized traction free crack length a_0, the LEFM theory predicts a straight line increase of strength from zero to infinity with decreasing crack size (Figure 2.10). A structural strength higher than the material tensile strength is unrealistic suggesting the break-down of the LEFM theory at the limit of small crack. Similarly, the classical simple strength theory ignoring the presence of cracks in a structure would predict a constant strength (horizontal line in Figure 2.10), again unrealistic from practical experience. On the other hand, the LEFM and strength theories have been proven adequate for ideally brittle Griffith type materials and for ductile yielding materials. These theories are therefore very useful ones in the limiting cases of suitably (will be explained later) large and small cracks respectively. Between these two limiting cases, we need a theory more suitable for the quasi-brittle material. The formalism presented in section 2.2 above can form the basis for such a non-linear fracture theory. This analysis results in the curve bridging the two limiting extremes, shown in Figure 2.10. The merging of this curve with those predicted by LEFM and material strength theories suggests the range of crack sizes when these simplified theories perform adequately.

The analysis presented above results in a natural "material characteristic length" l_{ch} parameter, defined as $G_C E/f_t^2$ or $(K_{IC}/f_t)^2$ where G_C is the fracture energy, K_{IC} is the fracture toughness, E the Young's Modulus and f_t is the tensile strength. The l_{ch} parameter was first introduced to concrete by Hillerborg [28] (with a slightly different definition of fracture energy). l_{ch} can be conveniently interpreted as the ratio between the slope of the stress-strain curve (the elastic Young's Modulus) and the slope of the tension-softening curve of a material if the tension-softening curve is approximated by a linear fit.

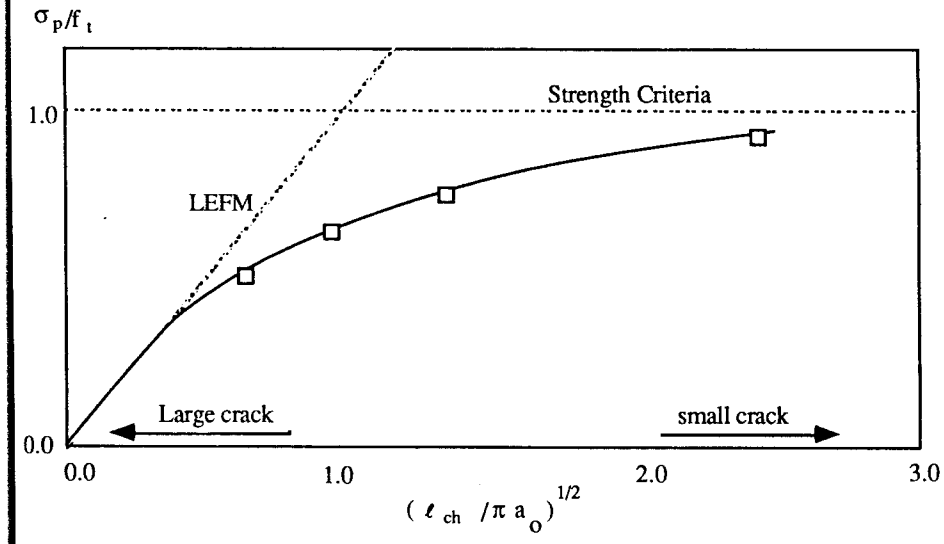

Fig. 2.10: Strength dependence on the relative crack length based on strength theory, linear elastic fracture mechanics theory and the present non-linear elastic fracture mechanics theory

The l_{ch} value of a quasi-brittle material is an extremely important material characterization parameter because it is a stronger indicator of brittleness than say the fracture energy or the fracture toughness itself. For example, the fracture toughness of high strength concrete and most ceramics would be higher than that for normal strength concrete, and yet these materials are generally perceived as more brittle than normal strength concrete. This is because the l_{ch} value for them is very small due to the disproportionate rise in tensile strength over fracture toughness. Hence the notch sensitivity increases from concrete, to high strength concrete to ceramics, due to their decreasing l_{ch} values. The contribution of fiber reinforcement or particle reinforcement in many such material systems is in the resulting disproportionate increase in toughness over tensile strength by providing an energy absorption process zone. [Note: the tensile strength and flexural strength in reinforced composites are not proportional. Toughness increase helps in the flexural strength but does not necessarily relate directly to the tensile strength.] For example, toughness increase in FRC is typically in the range of 10 to 50 times while strength increase is typically in the range of 1.1 to 2 times [2]. For ceramics composites, the toughness increase due to whisker and particulate reinforcements is typically in the range of 2 to 5 times while strength increase is typically not as significant [7].

In the concrete and rock community, there is increasing awareness that classical LEFM

based fracture tests often result in underestimation of the true fracture toughness value, reflected in a size dependence of fracture data. This is illustrated in Figure 2.11 using data collected by Francois [35] from concrete specimens. Figure 2.10 affords an explanation on why LEFM based fracture test which violates the small scale yielding criterion should be expected to yield lower than true fracture toughness. Suppose a measured specimen (structural) strength is used to interpret the fracture toughness using the dashed line strength prediction. This would give a smaller l_{ch} value than the actual value (obtainable from the strength curve based on non-linear analysis) for the same strength. Since the l_{ch} value is directly proportional to G_c, the toughness would be underestimated. Similar limitations to LEFM applied to rock tests have been suggested by Takahashi and Abé [36]. Figure 2.12 shows the size-dependence of the apparent fracture toughness of Indiana Limestone (from [37], see also [38]) and predictions made by Li [39] based on the type of non-linear fracture theory described above.

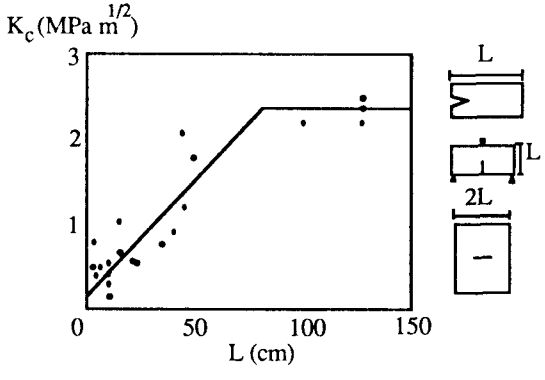

Fig. 2.11: Apparent fracture toughness data of concrete showing size dependence, adapted from [35]

It is often convenient to convert Figure 2.10 into a semi-log plot, as shown in Figure 2.13. The LEFM line will then have a slope of -0.5. Several sets of data (e.g. Bazant et al [40] who converted the horizontal axis to a non-dimensionalized 'structural size') have demonstrated that concrete as a quasi-brittle material follows the type of behavior predictable by a non-linear fracture theory which explicitly account for the presence of a bridging process zone.

The material characteristic lengths of some structural materials are given in Table 2.1. As an order of magnitude estimate, the process zone size may be regarded as roughly one to

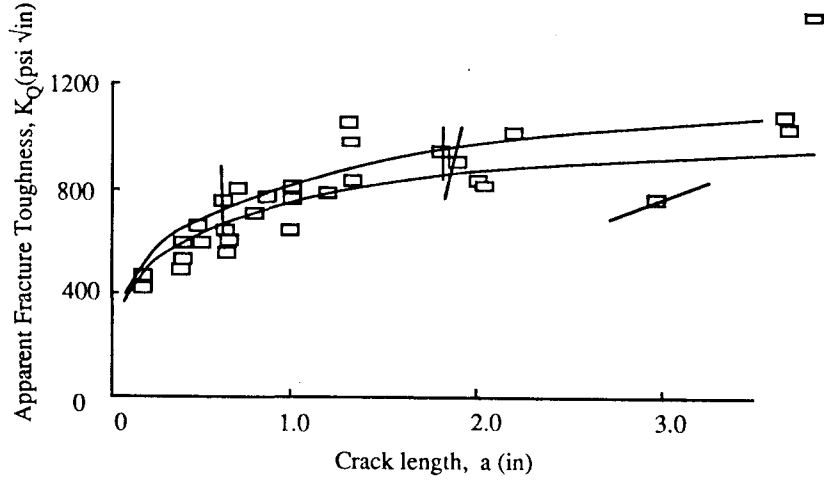

Fig. 2.12: Apparent fracture toughness of limestone showing size dependence, adapted from [37]. Lines are predicted size dependence from non-linear fracture mechanics theory

Table 2.1: Characteristic Length (l_{ch}) of some structural materials

Material	Material Characteristic Length (l_{ch}) in mm
Ceramics/Glass	
Monolithic Ceramics	0.02 - 0.4
SiC Whisker/Alumina (V_f=0.2)	0.27
SiC Fiber/LAS (V_f=0.45)	0.42
Carbon Fiber/Pyrex (V_f=0.4)	1.43
Cementitious Materials	
Concrete	60 - 160
High Strength Concrete	2 - 30
Fiber Reinforced Concrete	200 - 1000
Polymers	
Thermoplastics	0.3 - 20
Fiber Reinforced Thermoplastics	1.3 - 3
Thermosets	0.035 - 0.63
Fiber Reinforced Thermosets	1 - 25

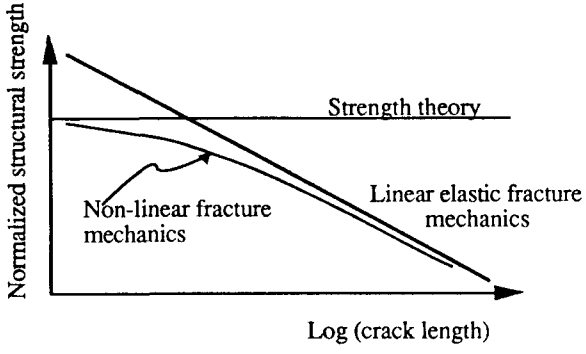

Fig. 2.13: Strength dependence on crack length

ten times that of the l_{ch} value. The exact value depends on, amongst other things, the shape of the tension-softening curve. This rough estimate may be useful in estimating the required minimum dimensions for LEFM based fracture tests, and in the determination of validity of LEFM based fracture analysis by comparisons to the minimum physical dimensions in a boundary value problem.

2.4 Concluding Remarks on Fracture Modelling in Quasi-Brittle Materials

In many inhomogeneous materials, formation of a crack tip process zone enhances the toughness of the material. Fracture analysis of structures of such materials by classical LEFM techniques may be hampered by the presence of such a process zone, if the zone size causes the small scale yielding condition to be violated. A non-linear formulation of fracture formation and propagation is reviewed for the case where the softening part of a force-displacement relation describing the process zone spring-type behavior is important. Results of a sample analysis suggest that the tension-softening curve for such a material is a fundamental property governing structural strength and R-curve behavior. For such materials, the material characteristic length l_{ch} is a useful indicator in determining the range of validity of the simpler LEFM theory.

The general σ_b-δ curve is fundamental in another sense. It directly reflects the material structure and processing conditions, and could be used as a measure of the effect or the effectiveness of microstructure tailoring in engineered advanced composite systems. Unfortunately techniques for measurement of the σ_b-δ curve is at present still not well developed although increasing amount of research in this area is inevitable. The following sections will look at theoretical models relating the material structures of fiber reinforced concrete to the composite tension-softening curve. Presentation of a new technique for

measuring the σ_b-δ curve based on the J-integral of Rice [17] applied to a quasi-brittle material concludes this chapter.

3. Tension-Softening and R-Curve Behavior in Fiber Reinforced Concrete

The introduction of fibers can significantly improve the fracture energy of concrete. Figure 3.1 [2] shows that with only one percent volume fraction of high modulus polyethylene fibers, the fracture energy improve by 600 times that without reinforcement. This toughness increase is mainly due to the alteration of the post-cracking behavior, enhancing the load bearing capacity even as the matrix crack opens. The resulting tension-softening curve of fiber reinforced concrete (FRC) is strongly influenced by the micromechanical failure mechanisms related to the specific type of fiber reinforcement.

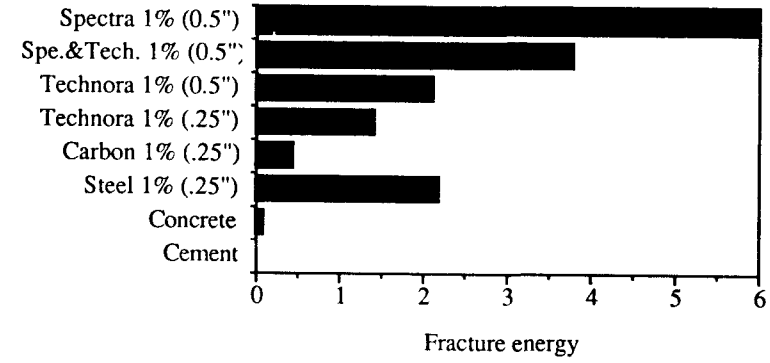

Fig. 3.1: Fracture energy of some synthetic FRC and other cementitious materials

The enhanced tension-softening process implies an enhanced bridging zone at a macroscopic crack tip in which energy is absorbed by fiber actions. These actions could include fiber pulled out against frictional work, fiber pulled out at an angle to the matrix crack as if going over a friction pulley (a snubbing process), and fiber elastically or inelastically elongated and/or ruptured. Some of these actions are most conspicuous in a high modulus polyethylene FRC [41] and may also occur in other composite systems. In this section we review a theoretical model [42] which combines the statistics of fiber distribution and the mechanics of fiber action to predict the tension-softening curve of such FRCs. It should be noted that the assumptions used in this model may not be applicable to other material systems. However, the model does serve to illustrate how a certain non-linear fracture resistance property of an inhomogeneous material could be predicted based on the material structure and failure mechanisms. This section ends with a discussion of the

effects of fiber pre-treatment on composite properties as indicated through an R-curve behavior analysis in relation to fiber bridging properties.

3.1 Composite Model

The following assumptions are adopted: (1) the fibers have 3-D random distribution in location and orientation; (2) the fibers are straight with cylindrical geometry; (3) the fibers behave linear elastically; (4) the fibers rupture when its axial stress reaches the fiber strength σ_f^u; (5) the Poisson's effect of the fiber on pull-out is neglected; (6) the fiber/matrix bond is frictional and the elastic bond strength is neglected. The frictional bond strength may exhibit slip hardening or weakening behavior. In addition, the model assumes that the effect of fiber pull-out from matrix at an oblique angle can be characterized by a snubbing friction coefficient, f.

Figure 3.2 shows a fiber of length L_f arbitrarily located with its centroid at a distance z from the matrix crack plane, and with an orientation angle ϕ to the tensile loading axis. Only fibers with a positive embedded length ℓ, defined by

$$\ell = \frac{L_f}{2} - \frac{z}{\cos\phi} \tag{3.1}$$

would cross the crack plane and provide the bridging action. For the case of uniform fiber length, the probability density function p(z) of the centroidal distance z is

$$p(z) = \frac{2}{L_f} \qquad for\ 0 \le z \le L_f/2 \tag{3.2}$$

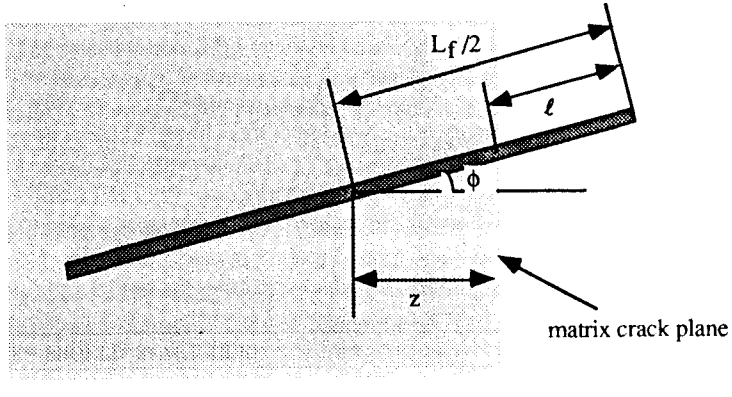

Fig. 3.2: A fiber crossing a matrix crack

For 3-D random orientation, the probability density function, $p(\phi)$, of the inclining angle ϕ is given by [42]

$$p(\phi) = \sin\phi \qquad for\ 0 \le \phi \le \pi/2 \tag{3.3}$$

The problem of two-sided fiber pull-out at ϕ=0 illustrated in Figure 3.3a will be described in the following section. For now, we turn our attention to the relationship of the force-displacement (P-δ) curve of a fiber arbitrarily oriented to that of a fiber with ϕ=0.

For a fiber with the same embedded length ℓ and with the same end slippage distance (s(0)), but with a non-zero inclining angle ϕ (Figure 3.3b), the bridging force will be increased. However, the distribution of the fiber axial force inside the matrix will still be the same for these fibers, irrespective of their inclining angles (ϕ). Using a snubbing friction coefficient, f, Li et al [43] related the bridging force for angle pull-out to that for ϕ = 0:

$$P|_\phi = e^{f\phi} P|_{\phi=0} \tag{3.4}$$

where f is an interface material parameter to be determined experimentally by single fiber pull-out test at various angles. The snubbing friction coefficients for nylon and polypropylene have been determined to be 0.99 and 0.70 respectively [43].

During the loading phase ($dP/d\delta \ge 0$), the crack separation for inclined fibers can be calculated from that of ϕ = 0 using superposition:

$$\delta|_\phi = \frac{P|_\phi - P|_{\phi=0}}{E_f A_f} L + \delta|_{\phi=0} \tag{3.5}$$

where E_f is the fiber elastic modulus, A_f is fiber cross sectional area, and L is the total slippage of the fiber ends. During unloading after reaching the peak load, part of the elastic elongation of the longer fiber embedded segment is recovered. The amount of the recovery depends on the snubbing friction force. Since the recovery occurs only after the shorter fiber segment has begun to slip out (i.e. when $s_1(0) > 0$), and the magnitude of this recovery is in general much smaller than the slippage distance, the recovery during unloading is neglected for simplicity. By so doing, $\delta|_\phi$ can always be determined from $\delta|_{\phi=0}$ for the same ℓ and L from (3.5), without the need of calculating the pull-out response directly for each ℓ and f. Equations (3.4) and (3.5) provide the P-δ relation (for any ϕ) sought for.

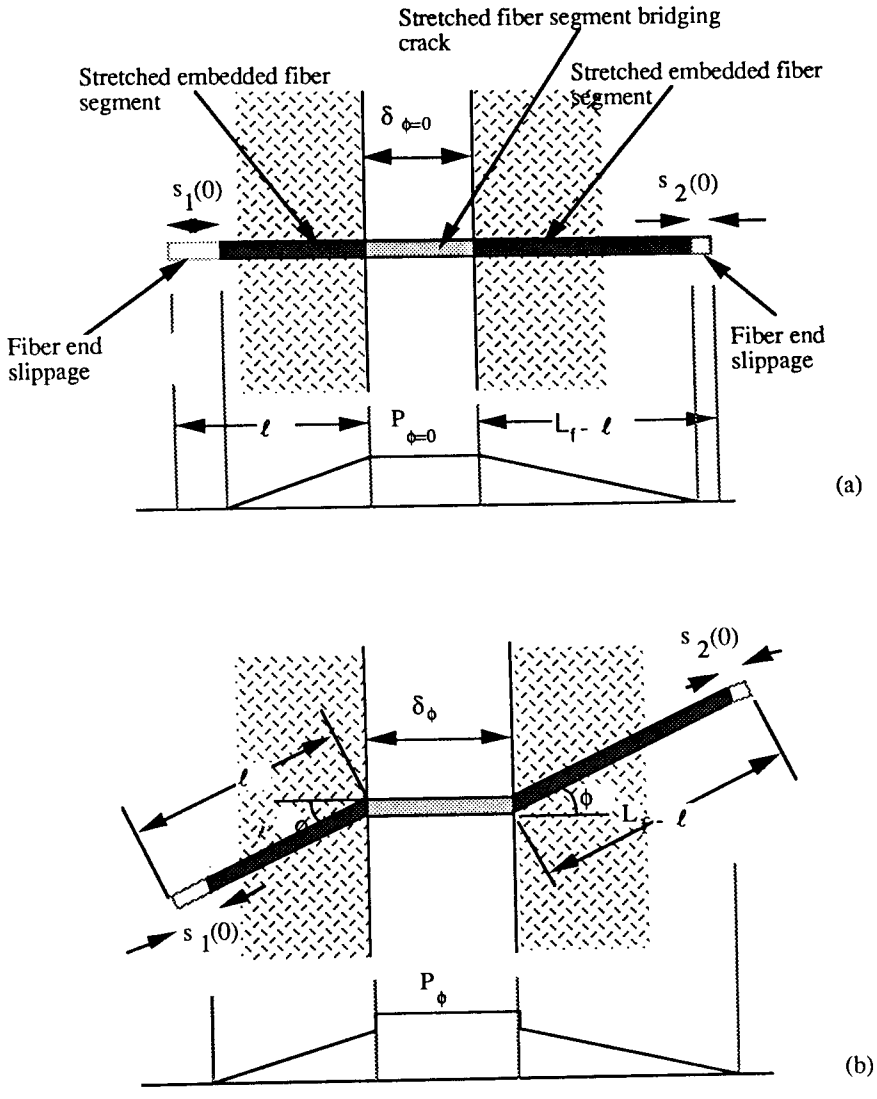

Fig. 3.3: (a) Two-sided fiber pull out for a fiber aligned in the direction of the tensile loading axis. The fiber has a length of L_f and a short embedded length of l, with end slippages $s_1(0)$ and $s_2(0)$. A bridging force P relates to a crack opening δ; (b) Two-sided fiber pull out for a fiber oriented at an arbitrary angle φ to the loading axis

To deduce the tension-softening curve for the composite, we may compute the traction transmitted across the matrix crack by integrating the force contributions from those fibers which are active in the bridging action. Thus for each crack opening δ, the composite bridging stress σ_b may be obtained from

$$\sigma_b = \frac{F}{A_c} = \frac{V_f}{A_f} \int_{z=0}^{L_f/2} \left[\int_{\phi=0}^{\arccos(2z/L_f)} P(\ell,\phi,\delta) p(\phi) d\phi \right] p(z) dz \qquad (3.6)$$

with p(z) and p(φ) given by (3.2) and (3.3). The integration limits in (3.6) exclude those fibers which do not cross the crack plane. The constituent parameters needed for (3.6) are (1) Fiber geometry -- diameter d_f and length L_f, (2) fiber properties -- elastic modulus E_f and fiber strength σ_f^u, (3) fiber volume fraction V_f, and (4) properties of fiber/matrix interface -- bond strength τ or slip-weakening/hardening law τ-s, and snubbing friction coefficient f. The fracture energy of the composite may be obtained by integration of (3.6) with respect to the crack opening. Equation (3.6) suggests that the $\sigma_b(\delta)$ scales with fiber volume fraction, and inversely with fiber diameter (since P varies linearly with d_f).

3.2 Single Fiber Pull-Out Model

The mechanics of pull-out of a single fiber embedded in a brittle matrix and aligned in the direction of tensile loading (Figure 3.3a) has been variously investigated, most notably in the form of shear lag models [e.g. 44, 45, 46, 47]. These models either assume that the debonded interface is traction free or is governed by a constant friction. In Wang et al [48,49], the model assumes a frictional bond at the fiber/matrix interface, neglecting any effect of an elastic bond due to expected low adhesion between polymer fibers and cement matrix. However, the frictional resistance is made to depend on the amount of slip so that either slip weakening or hardening phenomenon can be incorporated. In addition, the matrix is assumed to be much stiffer than the fiber and its deformation is neglected. The inclusion of slip-dependent frictional bond strength is motivated by observed fiber abrasion and the peculiar fiber pull out load-displacement curve measured for certain polymer fiber/cement matrix combinations.

The solution procedure of Wang et al [48,49] is illustrated in Figure 3.4 for the case of a slip-hardening frictional bond. In this case the short embedded end will be completely pulled out, whereas the long embedded end may have had some slippage. Geometric compatibility requires that $\delta = \delta_1 + \delta_2$ while equilibrium enforces the condition that $P_1 = P_2$. The latter condition implies that once the short fiber segment load P_1 decreases, the long fiber segment must also unload with partial retrieval of the slipped out segment back into the matrix, rather than following the complete direct pull-out curve indicated by the dashed line in Figure 3.4.

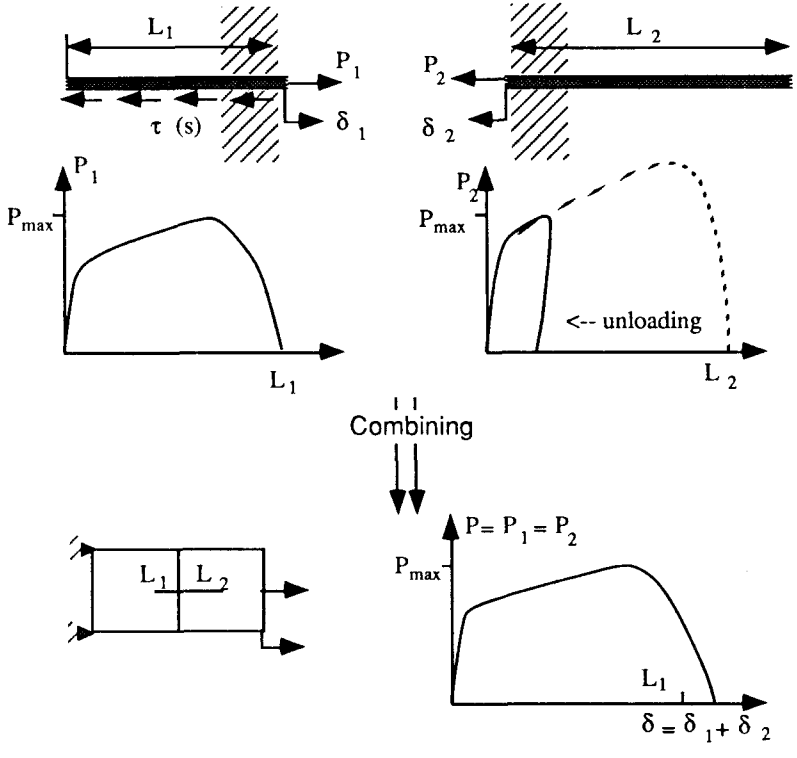

Fig. 3.4: Schematics of the modelling procedure

To analyze the direct pull-out problem, consider the shorter fiber segment of length L_1 before loading and during pull-out (Figure 3.5). The fiber slip s(x) at the material point x along the fiber length is given by the sum of the slippage distance of the fiber end s(0) plus the elastic elongation of the fiber segment between 0 and x:

$$s(x) = s(0) + \int_o^x \varepsilon(x)\,dx \tag{3.7}$$

where the axial strain ε(x) may be directly related to the axial force P(x):

$$\varepsilon(x) = \frac{4}{\pi d_f^2 E_f} P(x) \tag{3.8}$$

P(x) may be obtained from equilibrium considerations of a free body diagram of the fiber segment between 0 and x. Thus

$$P(x) = P_0 + \int_0^x \tau(x)\pi d_f\,[1+\varepsilon(x)]dx \tag{3.9}$$

and P_0 is a constant representing the fiber end anchorage effect when the fiber end slips ($P_0 = 0$ before complete debonding). The shear stress τ in general is a functional of local slip s(x) so that

$$\tau(x) = \tau(s(x)) \qquad \text{for } x + s(x) < L_1 \text{ (inside matrix)} \tag{3.10a}$$

$$\tau(x) = 0 \qquad \text{for } x + s(x) \geq L_1 \text{ (outside matrix)} \tag{3.10b}$$

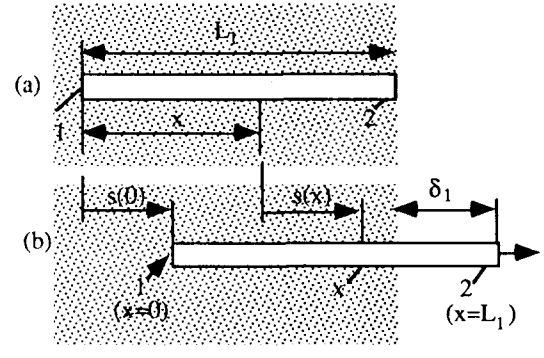

Fig. 3.5: Geometry (a) before and (b) during pull out of a fiber

Equations. (3.7) to (3.10) are in general coupled nonlinear equations and have to be solved numerically. At each loading stage, the load and the corresponding displacement at the exiting end of the fiber could be obtained from

$$P_1 = P(x = L_1) \tag{3.11}$$

$$\delta_1 = s(x = L_1) \tag{3.12}$$

To analyze the two sided pull-out problem, we now turn our attention to the behavior of the longer embedded fiber segment, illustrated in Figure 3.6. This fiber behaves exactly as described above for the shorter fiber segment, at least up to the maximum load P_{max}, after which unloading of this fiber occurs. Figure 3.6a illustrates the fiber condition at $P_2 = P_{max}$, and the slip distribution, the axial force and strain distribution at this state are labelled with a subscript m. In particular, the fiber axial force decreases from P_{max} at the exit end to

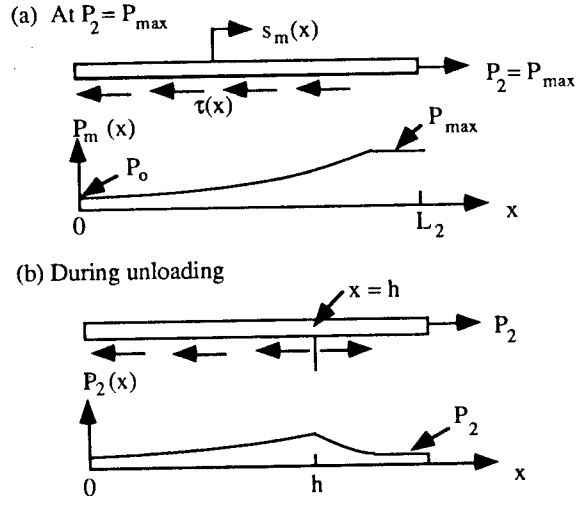

Fig. 3.6: Schematics of long embedded segment showing the state of fiber axial load distribution at (a) stage when short embedded segment reaches peak load; (b) subsequent stages when long segment has to unload

P_0 at the embedded end. During unloading, i.e. P_2 decreasing from its maximum value of P_{max}, part of the fiber retrieves back into the matrix against frictional resistance. Suppose the point x=h demarcates the boundary between the retrieving segment and the rest of the fiber which has not been affected by the unloading, then

$$P(x) = P_m(x) \qquad (x \le h) \tag{3.13}$$
$$\varepsilon(x) = \varepsilon_m(x) \qquad (x \le h) \tag{3.14}$$
$$s(x) = s_m(x) \qquad (x \le h) \tag{3.15}$$

For x>h, the axial force is found from the equilibrium conditions as:

$$P(x) = P_m(h) - \int_h^x \tau(x)\pi d_f[1+\varepsilon(x)]dx \qquad (x > h) \tag{3.16}$$

and the slippage distance at x is given by the slippage distance when $P = P_{max}$ plus the slippage distance due to fiber elastic unloading:

$$s(x) = s_m(x) + \int_h^x [\varepsilon_m(h) - \varepsilon(x)]dx \qquad (x > h) \tag{3.17}$$

Equations (3.8) and (3.10) are still applicable in describing the P-ε relation and the τ-s relation respectively for the retrieving fiber segment. Equations (3.13)-(3.17), together with (3.8) and (3.10) can be solved and the pull-out load and displacement at the fiber exit end can be determined:

$$P_2 = P(x = L_2) \tag{3.18}$$
$$\delta_2 = s(x = L_2) \tag{3.19}$$

By decreasing h from L_2 (no unloading when $P_2 = P_{max}$) until $P_2 = 0$, the P_2-δ_2 relationship for the unloading process can be obtained. The complete load versus crack separation curve P-δ is then calculated by adding the displacements of both short and long fiber segments together ($\delta = \delta_1 + \delta_2$) for the corresponding load ($P = P_1 = P_2$). This P-δ relationship is used (denoted as $P|_{\phi=0}$ and $\delta|_{\phi=0}$) in Equations (3.7) and (3.8) to compute the fiber load and crack separation for fibers with the same embedded length ($\ell = L_1$) and fiber length ($L_f = L_1 + L_2$) arbitrarily oriented to the loading axis.

Wang et al [48] represented the τ-s functional relationship in a quadratic form. They found that the model requires a slip-hardening representation in order to match data of certain synthetic fibers while a slip-weakening representation is required to match data of steel fibers. Figure 3.7 and 3.8 show the experimentally determined P-δ curves for a synthetic fiber and for a steel fiber pulled out from a cement matrix, and the corresponding model τ-s and predicted P-δ curves. The steel fiber pull-out data is from [50].

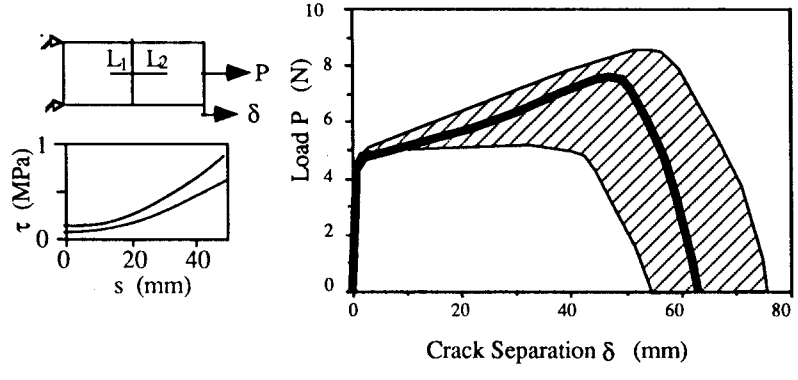

Fig. 3.7: Force-displacement relationship of single nylon fiber pulled out from a cement matrix. Experimental data (4 sets) fall in shaded area. Thick solid line is model prediction based on the slip-hardening curve shown in insert on left. Test configuration is also shown

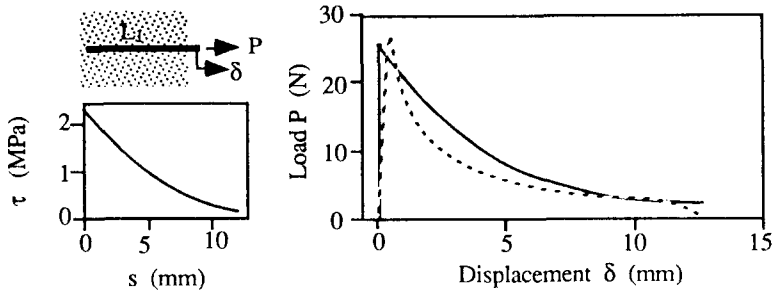

Fig. 3.8: Force-displacement relationship of single steel fiber pulled out from a cement matrix. Experimental data is shown as dotted line. Solid line is model prediction based on the slip-hardening curve shown in insert on left. Test configuration is also shown

3.3 Predicted Composite Tension-Softening Curve and Comparisons with Experimental Observations

As expected, the predicted composite tension-softening curves are sensitive to the nature of slip resistance (slip-hardening or slip-weakening), the fiber and matrix properties, and fiber geometry. A specific result was obtained for two mixes of high modulus polyethylene fiber reinforced mortar with material and geometric parameters given in Table 3.1. Both the model predicted curve and the experimentally determined curve based on a specially devised uniaxial testing technique [51,52] are presented in Figure 3.9. In Mix S1 the matrix material is a normal strength mortar with tensile strength of approximately 2.5 MPa. From SEM studies of the fracture surface, a large amount of surface spall was observed, while the high modulus polyethylene fibers appear not to be abraded [53]. In contrast, no spalling was observed in the high strength mortar matrix Mix SH with a tensile strength of approximately 3.4 MPa. Although abrasion of high modulus polyethylene fibers has been observed under the SEM [53] in a similar mix, the same constant bond strength as for Mix S1 was employed on account of the short length of the fiber used in the Mix SH. The experimental testing technique and data on bond strength of various synthetic fibers can be found in [43,54,55]. For the snubbing friction coefficient f, angle pull out data for polypropylene was used although a direct measurement of f of high modulus polyethylene fiber embedded in both types of mortar matrix would have been preferred.

The comparisons shown in Figure 3.9 suggest that the model predictions are reasonable, with the exception of the initial part of the curve for Mix S1 which may reflect the matrix spalling effect not accounted for in the model.

Table 3.1: Material and Geometry Parametric Values Used in the Prediction of the Tension-Softening Curves in Figure 3.9

Parameters	Mix S1	Mix SH
d_f (mm)	38	38
L_f (mm)	12.7	6.3
E_f (GPa)	120	120
σ_f^* (GPa)	2.6	2.6
V_f (%)	1	0.6
τ (MPa)	1.02	1.02
f	0.7	0.7

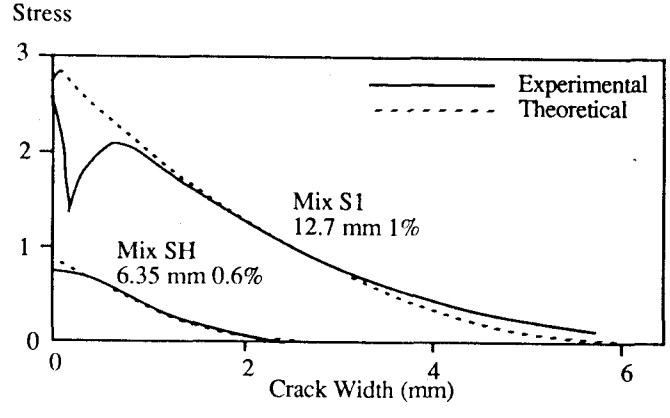

Fig. 3.9: Comparison of predicted and measured tension-softening curves for high modulus polyethylene fiber reinforced mortar. Mix S1 has a normal strength matrix. Mix SH has a high strength matrix

Li et al [42] found that the fiber length plays a significant role in controlling the composite behavior. When fiber length (for a given snubbing coefficient) is not long enough to cause fiber rupture, the fracture energy increases approximately quadratically with fiber length. However, long fiber length also implies more fiber ruptures and loss of reinforcement bridges. The result is a sharp drop shortly after peak load in the tension-softening curve and a corresponding reduction in fracture energy. Figure 3.10 shows the tension-softening curves schematically for three composites with everything identical except fiber length. The corresponding effect on the process zone bridging stresses is also illustrated.

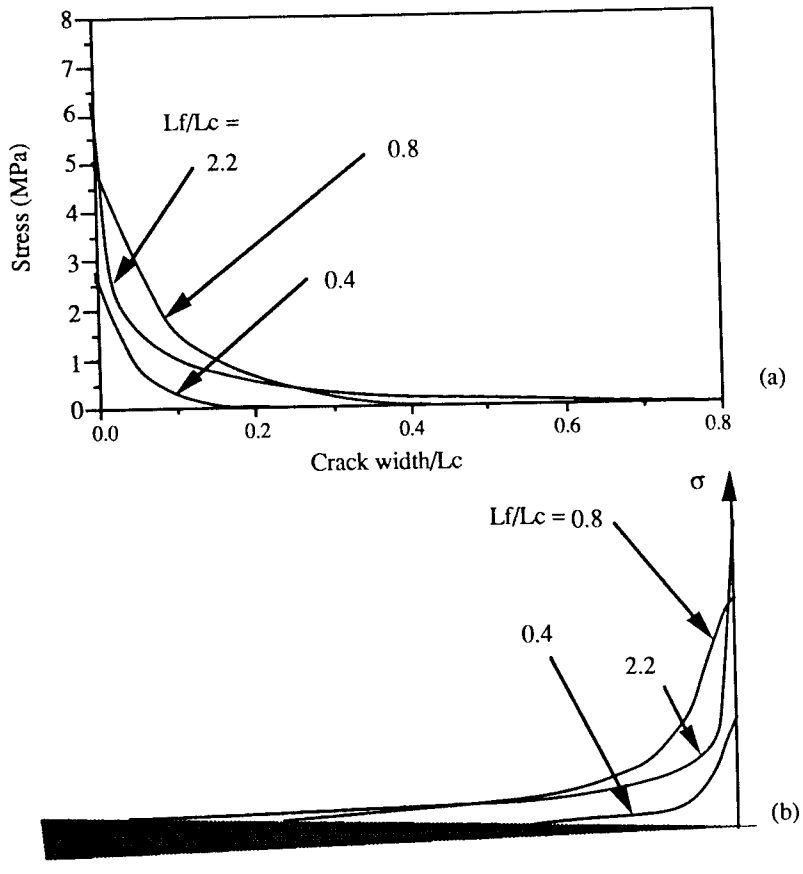

Fig. 3.10: Effect of fiber length on (a) the tension-softening curve and (b) the stress-distribution in the process zone. Fiber length is normalized by critical length L_c [43]

3.4 R-curve Studies

Because of the intimate relation between interfacial properties and the tension-softening curve, the relation between the tension-softening curve and process zone development, and the relation between process zone development and the R-curve (section 2.2), we now turn our attention to analyzing the R-curve of FRC in which fibers have been pretreated in order to change the interface properties. This discussion is based on a R-curve model for double cantilevered beam (DCB) specimen described in [56]. By treating the beams as undergoing pure bending, its compliance as a function of beam length (equal to the crack length) can be

computed from elementary beam theory. This allows the energy release rate and the stress intensity factor K_a to be related to the applied loading, the crack length, the elastic modulus and Poisson's ratio, and the polar moment of inertia of the beam cross section. Similarly, the stress intensity factor, K_b, at the matrix crack tip due to fiber bridging stresses $\sigma_b(x)$ acting as a closing pressure was found to be

$$K_b = -\int_{a_0}^{a} \sigma_b(x) b(a-x)\left[bI\left(1-\nu^2\right)\right]^{-1/2} dx \tag{3.20}$$

where a_0 is the traction-free crack length. For equilibrium crack growth in the matrix, the total stress intensity factor, $K_a + K_b$, can be considered to be equal to the matrix toughness, K_m:

$$K_a + K_b = K_m \tag{3.21}$$

For a given load, solving (3.21) requires an iterative process to find the crack length, a. Once a is found, the corresponding composite fracture energy, G, can be calculated from

$$G = \int_{a_0}^{a} \sigma(x) \frac{\partial \delta(x)}{\partial x} dx + \frac{1-\upsilon^2}{E} K_m^2 \tag{3.22}$$

and the crack resistance, K_R, from $K_R = [EG/(1-\nu^2)]^{1/2}$. Note that when the process zone becomes fully developed, K_R will reach its steady state value, and the corresponding G is given by

$$G = \int_0^{\delta^*} \sigma(\delta) d\delta + \frac{1-\upsilon^2}{E} K_m^2 \tag{3.23}$$

where the integral part is simply the area under the σ_b-δ curve and $\sigma_b(\delta)=0$ when $\delta > \delta^*$.

This model was used to study R-curve measurement of Visalvanich and Naaman [57,58] in steel FRC tapered DCB. Typical values of E=21.5 GPa, ν=0.18, and K_{IC}=1 MPa $m^{1/2}$ for the matrix and experimentally determined σ_b-δ curve reported in [58] were used for the calculation. Depending on the choice of I_{min} or I_{max}, which correspond to the smallest and largest cross-sections of the DCB respectively, in the calculation, different R-curves were obtained. Their experimental data fall essentially in between these two limiting curves (Figure 3.11). As expected, for small crack extension (Δa), the experimental data lie closer to the R-curve for I_{min}, and for large Δa, the data bend toward the curve for I_{max}.

The tension-softening curves for three composites reinforced with one percent nylon monofilaments was approximated as shown in Figure 3.12a based on single fiber pull-out test for three pretreated fibers [54]. Case 1 was prewashed in hot water to remove the oil

finish and may have enhanced the abrasion effect. Case 2 was coated with a fluorocarbon mold release agent to reduce the frictional resistance against sliding of the interface. Case 3 was mechanically crimped by running the fiber between a set of gears. In this case the pull-out resistance is significantly improved and could lead to fiber rupture during the pull-out process. The predicted R-curve based on the theoretical model described above together with these bridging σ_b-δ curves are shown in Figure 3.12b. It is seen that in all cases, the bridging zone contribution to fracture toughness far exceeds that of the matrix toughness.

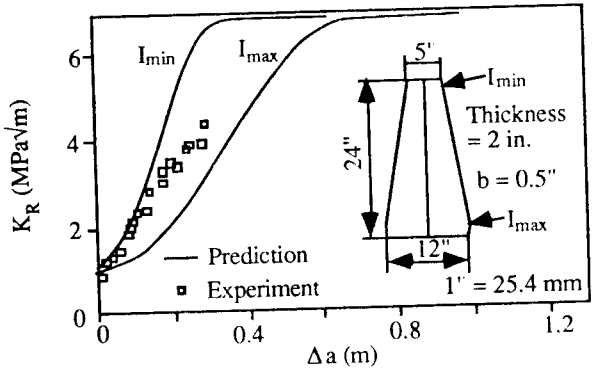

Fig. 3.11: Predicted and experimentally determined R-curve of steel FRC DCB

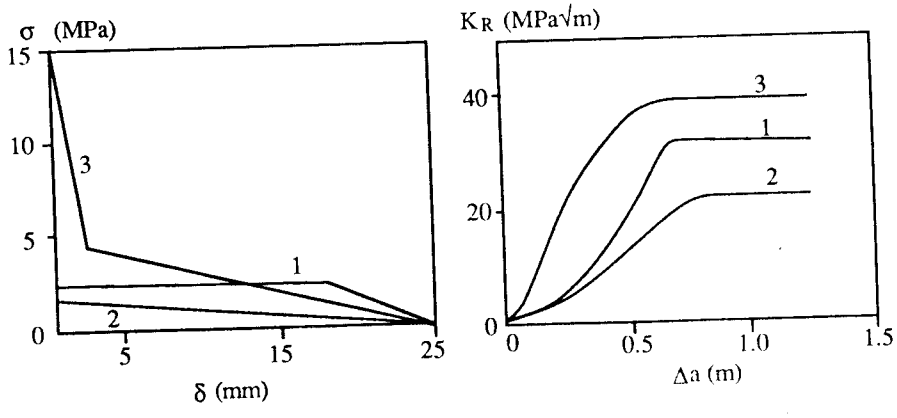

Fig. 3.12: (a) FRC σ–δ curves with fiber pre-treatment for 1) pre-washed, 2) fluorocarbon agent coated & 3) mechanically crimped, (b) corresponding predicted R-curves

Comparison between case 1 and 2 indicates that the surface finish can amount to a 50% change in fracture toughness. Case 3 suggest that mechanical interlock due to fiber crimps could lead to further increase in composite fracture toughness. In addition, the rise of apparent fracture toughness is much more rapid so that cracks could be arrested at an early stage before a long length is developed.

3.5 Concluding Remarks on Tension-Softening Models of FRC

This section discusses a theoretical model of post-peak behavior of short fiber reinforced brittle matrix composites with particular attention to the tension-softening behavior of synthetic fiber reinforced concrete, for which comparisons were made between experimental data and theoretical predictions. The model accounts for several physical processes related to the material structure and which appears to govern the tensile properties in such composites. These physical processes include the effect of fiber abrasion during fiber pull-out and result in a slip-hardening interfacial bond strength, as well as a snubbing effect exhibited during fiber withdrawal inclined to the matrix crack. The randomness of the fiber location and orientation is accounted for statistically. It is found that composite tension softening curve is strongly influenced by the slip-hardening behavior and fiber length.

A simple R-curve model is reviewed. This model was used to make predictions of R-curves based on various tension-softening relations. The effect of fiber treatment on R-curve behavior was discussed and found to play a significant role in determining composite toughness and the shape of the R-curve.

4. EXPERIMENTAL DETERMINATION OF TENSION-SOFTENING CURVES FOR QUASI-BRITTLE MATERIALS

In section 2, the post-cracking tension-softening behavior has been shown to control the growth of fracture in quasi-brittle materials. Section 3 presents a model of tension-softening curve for fiber reinforced concrete in relation to its failure mechanisms and phrased in terms of the material structure. In this section, we discuss methods for the experimental determination of tension-softening curves for quasi-brittle materials. Much of the examples are given for concrete and fiber reinforced concrete, but the test methods and particularly, the principals behind them are expected to be useful for other quasi-brittle materials such as rock and ceramics as well.

Two main classes of test are described. The first class involves the direct uniaxial test, and the second involves a special technique which employs non-linear elastic fracture theory to manipulate flexural type test data into tension-softening curves.

4.1 Uniaxial Tension Test

4.1.1 Stability and Other Considerations:

The uniaxial tension test is the most direct way of obtaining the uniaxial tensile behavior in any material. However, its application to obtaining the post-cracking tensile behavior have several demanding requirements which are difficult and not always met by measuring techniques. These requirements include [51]:

1. The testing fixture, including the testing machine, the loading grips, and the junctions between them, must be stiff so as to avoid unstable unloading after the specimen peak load is reached;

2. Misalignment of the specimen should not be introduced by the loading grips to avoid imposition of an unknown initial stress field on the specimen;

3. The testing fixture should have high rotational rigidity to prevent bending strains in the specimen and thus to ensure a uniform strain across the specimen.

The first requirement is related to the concept of stability. Figure 4.1 illustrates the chain of load transfer from machine to grips/fixtures to the specimen and finally to the fracture surface. One may conceptualize that the load is transferred through an effective spring with a certain compliance c (or inversely stiffness k = 1/c) contributed by a collective 'loading system' comprised of the testing machine, the loading grips, junctions between them as well as the volume of specimen material outside the fracture zone. During the

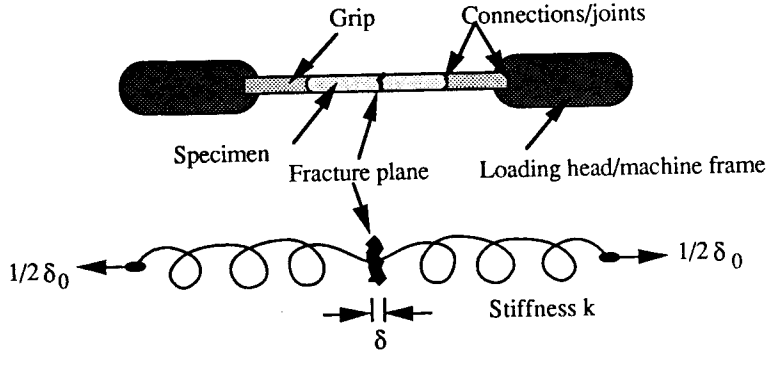

Fig. 4.1. Schematics of load transfer from machine to fracture plane. The loading system is conceptualized as a spring with stiffness k, with load point motion described by δ and the fracture plane opening by amount δ_0

tension-softening process as the crack plane opens, the load is continually reduced, and the loading system must unload to maintain equilibrium. This process may be represented graphically as following unloading lines with slopes determined by the loading system stiffness (Figure 4.2a). When the loading system is compliant, the unloading lines are closer to being flat on a plot of load (stress) versus displacement. When the loading system is stiff, the unloading lines are closer to being vertical. In the unloading stage, the constitutive relation of the fracture plane may be represented by its tension-softening curve. The load point displacements δ_0 and fracture plane opening δ for each system are traced in Figure 4.2b, indicating a loss of stability when the unloading stiffness matches the slope of the tension-softening curve for a compliant system.

For the above reasons, attempts at stiffening machines have been made by several researchers. Petersson [59] used two parallel columns which were heated to act as a displacement controlled loading machine. Reinhardt [60] used electronic control to carry out cyclic loading by monitoring the load drop of the load cell. Gopalaratnam and Shah [61] used a electronic feedback system which monitor the crack opening. These techniques met with various degrees of success in making a stiff loading system. It should be mentioned that the load system also involves the specimen volume. Large specimen volume contributes to a reduced system stiffness and should therefore be avoided.

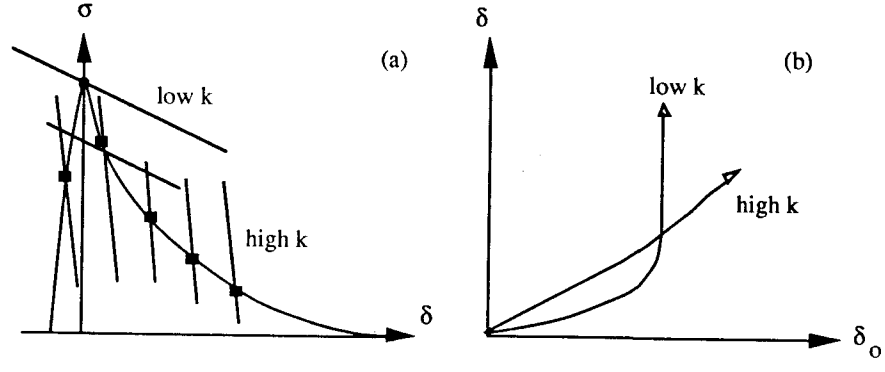

Fig. 4.2. Stability consideration during the unloading process. (a) Unloading lines with slope corresponding to spring stiffness k are superimposed on fracture plane tensile constitutive behavior. Points of equilibrium are indicated by square dots. A point of instability occurs for the spring with low k at the stage indicated by a circular dot. No instability occurs for the spring with high k. (b) Trace of load point displacement plotted against fracture plane opening. For the spring with low k, the fracture plane opening accelerates to infinity as instability is approached

The issues of system stiffness, system alignment and rotational rigidity are each discussed in [51]. Here we note that the problem of alignment often contributes to a reduction in measured tensile strength. This problem is particularly serious in brittle material sensitive to edge flaws which propagate across the specimen when bending stresses are introduced. Thus what is measured is really the residual strength of an unintentionally notched specimen under bending loads rather than the true tensile strength. In a tougher material such as composites with adequate fiber reinforcements, traction is maintained across an initiating crack, so that this problem may be expected to be less serious. In the following, we discuss an especially simple test technique used by Wang et al [51] for synthetic fiber reinforced concrete. Test methods and data for ceramics can be found in [62], for rocks in [62], for fiber reinforced thermoplastics in [4].

4.1.2 Test Set-up and Results:

The test set-up employs a 1331 servo-hydraulic Instron machine of 100 kN tension/compression capacity. The loading fixture consists of a pair of heavy steel plates tightly connected to the testing machine. One plate is bolted to the load cell and the other to the actuator piston, as illustrated in figure 4.3. The test specimen is glued to the loading plates with fast curing epoxy adhesive. By elimination of "soft" connections between specimen and machine, this set-up reduce the system compliance to a minimum as well as providing the maximum restrain from end rotation. In addition, the in-situ curing of the adhesive excludes non-uniform initial strains in the specimen with close to perfect alignment.

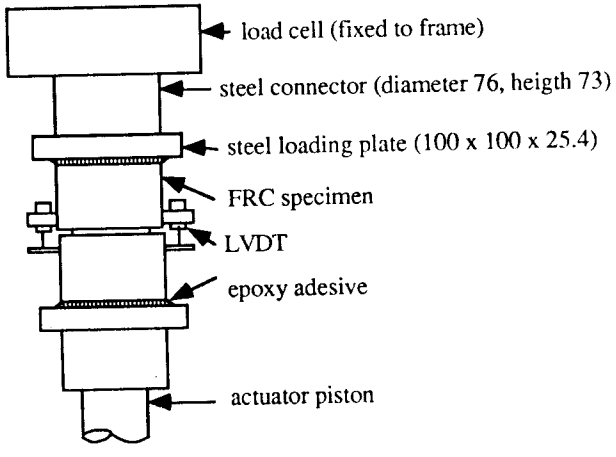

Fig. 4.3. Schematic illustration of loading fixture. Dimensions are in mm

Two LVDTs (linear variable differential transducers) were used to monitor the crack opening displacement, both with a displacement range of 5.08 mm. The LVDTs were mounted on two opposite sides of the specimen with aluminum holders glued to the specimen surface. The nominal measuring gage length was 12.7 mm. Signals of load, crack openings of the two sides, and the machine piston displacement were recorded by a micro computer. The test was performed at constant speeds of machine piston movement. Comparisons of the two LVDTs on either side of the specimen indicated no noticeable bending effect in the specimen. Details of specimen preparation and testing procedure can be found in [51].

After completing a uniaxial tension test, the data should be interpreted as shown in Figure 4.4. Correction for elastic behavior could be important for a material like concrete, but is likely to be unimportant for fiber composites. The tension-softening curves obtained using the method described above for several synthetic FRCs are given in Figure 4.5. Interpretations of the shape of these tension-softening curves in relation to material microstructures and failure mechanisms are given in [41]. Despite the successful use of this simple method in fiber reinforced concrete, its application to fiber reinforced high strength concrete and to mortar have met with difficulty, either due to inadequate machine stiffness or due to machine inaccuracy in displacement control, or both. An alternative method perhaps more suitable for quasi-brittle material with smaller material characteristic length lch than fiber reinforced concrete is described below.

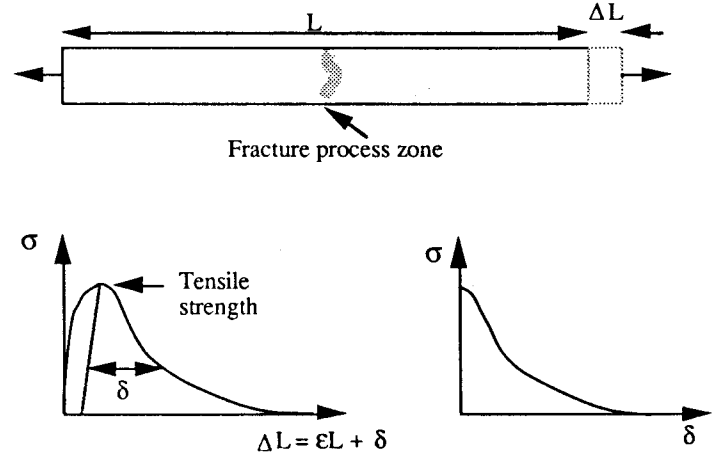

Fig. 4.4. Procedure for deduction of tension-softening curve from uniaxial tension test data of a quasi-brittle material.

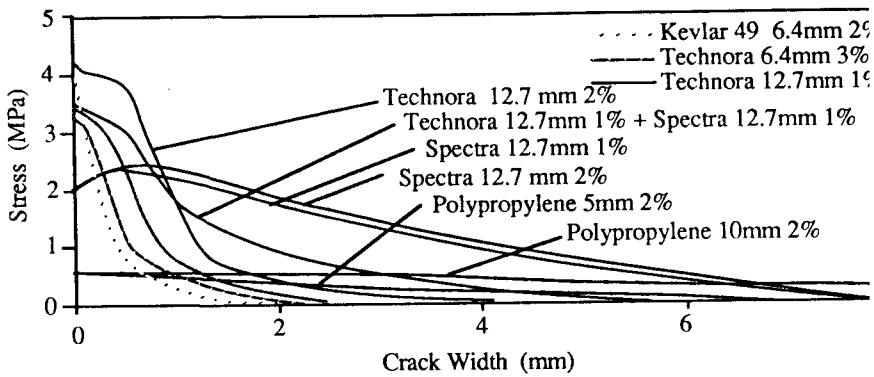

Fig. 4.5. Tension-softening curves for several mixes of synthetic FRC

4.2. Indirect Tension Test

The indirect tension test developed by Li and co-workers [64, 65, 66, 67, 68] for measurement of tension-softening curves of quasi-brittle materials, has so far been app to mortar, fiber reinforced mortar and rock [69, 70]. Development of this method for ceramics is now ongoing.

4.2.1 Theoretical Considerations

The path independent J-integral is defined as:

$$J = \int_{\Gamma}\left(Wdy - \underset{\sim}{T}\frac{\partial \underset{\sim}{u}}{\partial x}ds\right) \tag{4.1}$$

where Γ is a curve surrounding the notch tip, W is the strain energy density, $\underset{\sim}{T}$ is the traction vector in the direction of the outward normal along Γ, $\underset{\sim}{u}$ is the displacement ve and ds is an arc along Γ. From (1.4), Rice [17, 71] produced two alternative definitic J. He used the Barenblatt approach which considers a cohesive zone ahead of the crac in which the restraining stress $\sigma_b(\delta)$ is viewed as a function of separation δ. In a ten softening material (Figure 2.3c, $K_m = 0$) this would be the tension-softening curve in bridging zone. If the J-integral is evaluated along a contour Γ_1, shown in Figure 2.4, which runs alongside the bridging zone, then

$$J = \oint_{\substack{\text{bridging}\\ \text{zone}}} \sigma_b(\delta)\frac{d\delta}{dx}dx \tag{4.2}$$

where B is
is also mea
Differentiat

$$\sigma_b(\delta) =$$

and the ten

4.2.2 Num

This metho
configurati
employing
point displ
specimens
for the ten
the exercis
numerical
curve, thu
carry out
displacem
shows the
results are

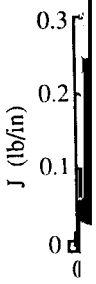

Fig.

shows average crack opening values, δ_1, δ_2 expressed as a function of load point displacement Δ. δ_1 was measured at the initial crack tip, δ_2 at a point 6.35 mm (equal to Δa) above the crack tip, both in the short cracked beams. The crack separation used in the procedure described above is then obtain from the average $\delta = (\delta_1 + \delta_2)/2$. A J-$\Delta$ relationship was calculated using numerical integration. This result combined with the Δ-δ relation provides the J-δ curve, as shown in Figure 4.11. Numerical differentiation of the J-δ curve was achieved using Taylor expansions at five consecutive points J(δ-g), J(δ-h), J(δ), J(δ+j), J(δ+k) and solving for J'(δ). Figure 4.12 shows the deduced tension-softening curve. It shows an initial rise from σ_b=0 to σ_b=f_t before descending back down to σ=0. The area under this initial ascending part may be interpreted as the lumped energy consumed by the fracture resistance of the matrix and the rising part of the spring law (see Figure 2.3) prior to the formation of bridging action in the fracture process zone and therefore should not be regarded as part of the tension-softening σ_b–δ relationship. Figure 4.13 shows the corrected σ_b–δ curve as well as the curve obtained from the direct tension test. The agreement is reasonably good. Test curves for other materials based on this method is shown in Figure 4.14. Further comparisons with direct tension-test results could be found in [66].

A major disadvantage of the method just described is the need for data differentiation which often exaggerates any error encountered in the experimentally recorded data. For this reason, it is recommended that a direct uniaxial tension test be carried out for the tensile strength of the same material for use as an accuracy control.

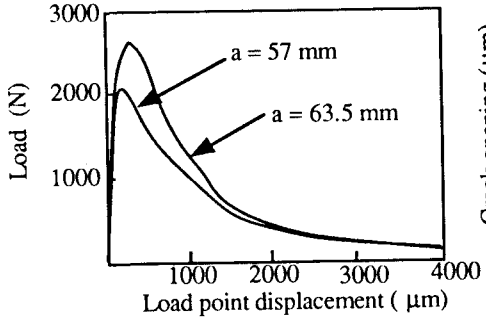

Fig. 4.9. Load vs load displacement

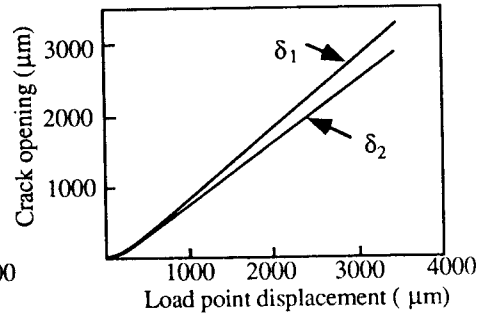

Fig. 4.10. Load displacement vs crack opening

4.2.4. Concluding Remarks on Tension-Softening Curve Measurements

Two types of experimental techniques for the determination of the tension-softening curves for quasi-brittle materials are described. Each has their own advantage and

disadvantages. Results from the direct tensile test is easy to interpret, but the test is difficult to carry out especially for quasi-brittle material with high strength or low l_{ch}. An alternative test method using non-linear fracture mechanics theory could be used to indirectly determine the tension-softening curve. This method has been numerically and experimentally verified for several quasi-brittle material and for several testing configurations.

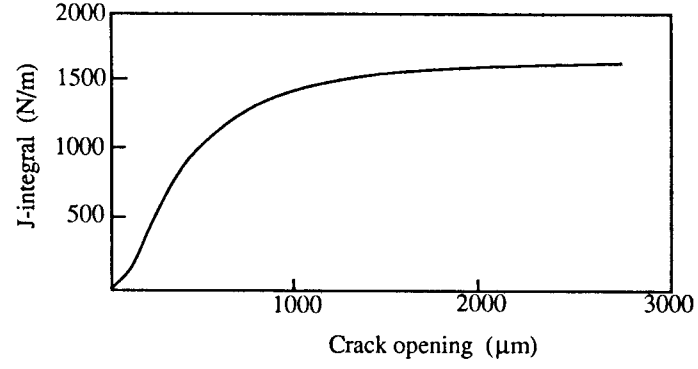

Fig. 4.11. J-integral versus crack opening curve

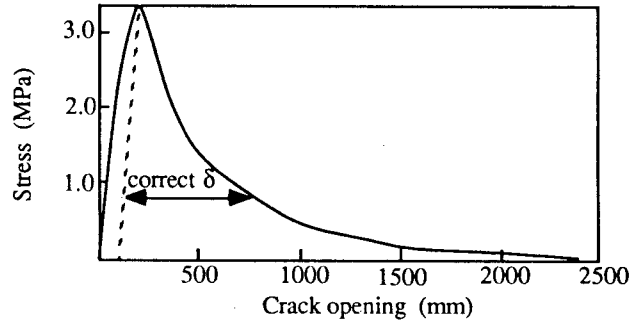

Fig. 4.12. Deduced tension softening curve

5. FINAL REMARKS

This chapter presents the theory of non-linear fracture mechanics of inhomogeneous quasi-brittle composites. Non-linear spring laws are used to describe the closing pressure acting on the crack flanks in the crack tip process zone. It is shown that such spring laws control the development of the fracture process, leading to the possibility of large scale 'yielding', and invalidating the use of linear elastic fracture mechanics.

From a materials performance point of view, it is suggested that the bridging spring action can substantially elevate the material toughness, thus motivating the attempt to relate material structure to the tension-softening spring law. While such models may provide a rational foundation and potential of systematically tailoring the material structure to improved material performance, much more research is needed and expected.

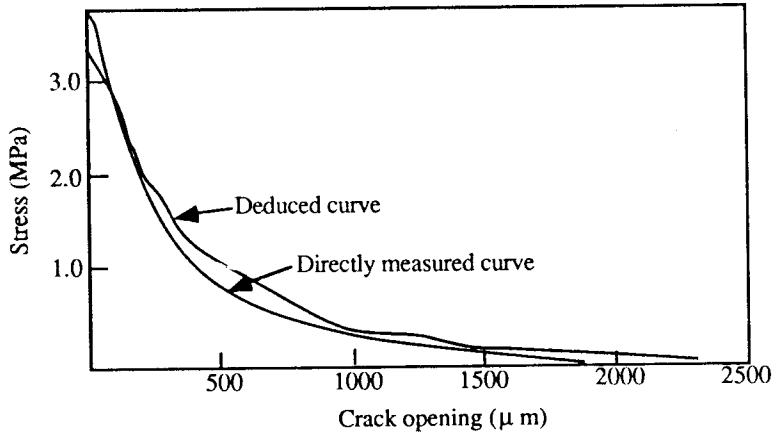

Fig. 4.13. Comparison between directly measured and deduced tension-softening curves

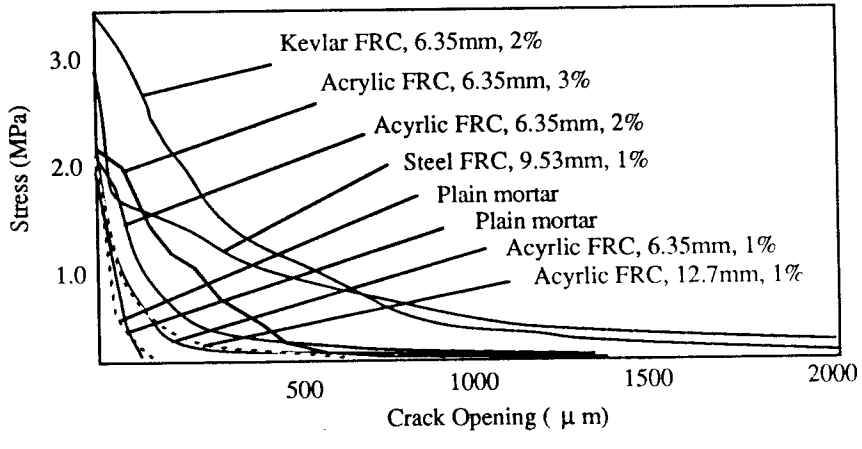

Fig. 4.14. Tension-softening curves of several quasi-brittle materials measured by the indirect J-integral based technique

Finally, the need to have a simple means of measuring the spring law for a given quasi-brittle material system cannot be overstated. Such development should help in providing constitutive relationship for modelling structural behavior on the one hand, and also assist in evaluating the post-cracking performance in inhomogeneous quasi-brittle materials.

ACKNOWLEDGEMENTS

This work is based on the research results of several projects which have been made possible by the generous support of the United States National Science Foundation, the United States National Aeronautics and Space Adminstration and the Shimizu Corporation. Helpful discussions with many individuals, particularly my colleague S. Backer, and former graduate students E. Green, J. Huang, Y. Kaneko, C. Leung, Y. Wang, and R. Ward are especially acknowledged.

REFERENCES

1. Diamond, S. and A. Bentur: On the Cracking in Concrete and Fiber Reinforced Cements, in: Application of Fracture Mechanics to Cementitious Composites (Ed. S.P. Shah), Martinus Nijhoff Publ., 1985, 87-140.

2. Li, V.C., S. Backer, Y. Wang, R. Ward, and E. Green: Toughened Behavior and Mechanisms of Synthetic Fiber Reinforced Normal Strength and High Strength Concrete, in: Fiber Reinforced Cements and Concretes, Recent Developments (Eds. R.N. Swamy and B. Barr), Elsevier Applied Science, London, 1989, 420-433.

3. Mandell, J., Darwish, and F. McGarry: Fracture testing of injection-molded glass and carbon fiber-reinforced thermoplastics, ASTM STP 734 (1981), 73-90.

4. Jang and Liu: Fracture behavior of short-fiber reinforced thermoplastics, I: crack propagation mode and fracture toughness, J. Appl. Poly. Sci., (1985), 3925-3942.

5. Becher, P.F., C.H. Hsueh, P. Angelini, and T.N. Tiegs: Toughening behavior in whisker-reinforced ceramic matrix composites, J. Am. Soc., 71, 12 (1988), 1050-1061.

6. Ruhle, M., B.J. Dalgleish, and A.G. Evans: On the toughening of ceramics by whisker, Scrip. Metal., 21 (1987), 681-686.

7. Evans, A.: The New High Toughness Ceramics, SB report, 87.

8. Mindess, S.: The Application of Fracture Mechanics to Cement and Concrete: A Historical Review, in: Fracture Mechanics of Concrete (Ed. F.H. Wittmann), Elsevier Publ., 1983, 1-30.

9. Swanson, P.L.: Crack-interface Traction: A Fracture-Resistance Mechanism in Brittle Polycrystals, in: Advances in Ceramics, Am. Ceram. Soc., Columbus, OH, 1986.

10. Swanson, P.L., C.J. Fairbanks, B.R. Lawn, Y.W. Mai, and B.J. Hockey: Crack-interface grain bridging as a fracture resistance mechanism in ceramics: I, experimental study on alumina, J. Am. Ceram. Soc., 70, 4 (1987), 279-289.

11. Sakai, M., J. I. Yoshimura, Y. Goto, and M. Inagaki: R-Curve behavior of a polycrystalline graphite: microcracking and grain bridging in the wake region, J. Am. Ceramic Soc., 71, 8 (1988), 609-616.

12. Reichl, A. and R.W. Steinbrech: Determination of crack-bridging forces in alumina, J. Am. Ceram. Soc., 71, 6 (1988), 299-301.

13. Kramer, E.J.: Microscopic and Molecular Fundamentals of Crazing, in: Crazing in Polymers, Advances in Polymer Science 52/53, (Ed. H.H. Kausch), Springer-Verlag, 1983, 1-56.

14. Budiansky, B.: Micromechanics II, in: Proceedings of Tenth U.S. Congress of Applied Mechanics, 1986.

15. Rose, L.R.F.: Crack reinforcement by distributed springs, J. Mech. Phys. Sol., 35 (1987), 383-405.

16. Marshall, D.B., and A.G. Evans: The influence of residual stress on the toughness of reinforced brittle materials, Material Forum, 11 (1988), 304-312.

17. Rice, J. R.: Mathematical Analysis in the Mechanics of Fracture, in: Fracture: An Advanced Treatise, 2, Academic Press, (1968), 191-311.

18. Rose, L.R.F.: Toughening due to crack-front interaction with a second-phase dispersion, Mech. of Mat., 6 (1987), 11-15.

19. Rice, J. R.: Crack Fronts Trapped By Arrays of Obstacles: Solutions Based on Linear Perturbation Theory, in: Analytical, Numerical, and Experimental Aspects of Three Dimensional Fracture Processes, AMD-91, (Eds. A.J. Rosakis, K. Ravi-Chandar, Y. Rajapakse), ASME, 1988, 175-184.

20. Irwin, G.R.: Analysis of stresses and strains near the end of a crack traversing a plate, J. Applied Mechanics, 24 (1957), 361-364.

21. Barenblatt, G.I.: Mathematical Theory of Equilibrium Cracks in Brittle Fracture, in: Advances in Applied Mechanics, VII, Academic Press, New York, 1962.

22. Dugdale, D.S.: Yielding of steel sheets containing slits, J. Mechanics and Physics of Solids, V.8, 1960.

23. Marshall, D.B. and B.N. Cox: A J-Integral method for calculating steady-state matrix cracking stresses in composites, Mechanics of Materials, 7 (1988), 127-133.

24. Li, V.C. and E. Liang: . Fracture process in concrete and fiber reinforced cementitious composites, ASCE J. of Engineering Mechanics, 112, 6 (1986), 566-586.

25. Palmer, A.C. and J.R. Rice: The Growth of Slip-Surfaces in the Progressive Failure of Overconsolidated Clay Slopes, Proceedings of the Royal Society of London, A332, (1973), 572-548.

26. Leung, C.K., and V.C. Li: Reliability of First-Cracking Strength for Short-fiber Reinforced Brittle Matrix Composites, In: Ceramics Eng. Sci. Proc., 9/10, 1989, 1164-1178.

27. Marshall, D.B. and A.G. Evans: Tensile Strength of Uniaxially Reinforced Ceramic Fiber Composites, in: Fracture Mechanics of Ceramics, (Eds. R.C. Bradt, A.G. Evans, D.P.H. Hasselman and F.F. Lange), 7 , Plenum Press, New York (1986), 1-15.

28. Hillerborg, A., M. Modeer, and P.E. Petersson: analysis of crack formation and crack growth in concrete by means of fracture mechanics and finite elements, Cement and Concrete Research, 6, (1976), 773-782.

29. Ingraffea, A. and W.H. Gerstle: Nonlinear Fracture Models for Discrete Crack Propagation, in: Applications of Fracture Mechanics to Cementitious Composites, NATO ASI Series, 94 (Ed. S.P. Shah) Martinus Nijhoff Publ., 1985, 247-286.

30. Ingraffea, A.: Theory of Crack Initiation and Propagation in Rock, in: Fracture Mechanics of Rock, (Ed. B. Atkinson), Academic Press, 1987, 71-110.

31. Mai, Y. and B. Lawn: Crack-interface grain bridging as a fracture resistance mechanism in ceramics: ii theoretical fracture mechanics model, J. Am. Ceram. Soc. 70, 4 (1987), 289-294.

32. Swanson, P.L.: Tensile fracture resistance mechanisms in brittle polycrystals: an ultrasonics and in-situ microscopy investigation, J. Geophysical Res., 92, (1987),

8015-8036.

33. Wecharatana, M. and S.P. Shah: Slow crack growth in cement composites, J. Stru., ASCE, 108, 6, (1982), 1400-1413.

34. Cook, R.: Transient Fracture Resistance in the Weak Toughening Limit, in: International Congress of Fracture, Proceeding Vol. 4, (Eds. Salama, Ravi-Chandar, Taplin, and Rao), 1989, 2747-2756.

35. Francois, D.: Fracture and Damage Mechanics of Concrete, in: Application of Fracture Mechanics to Cementitious Composites, (Ed. S.P. Shah) Martinus Nijhoff Publ., 1985, 141-156.

36. Takahashi, H. and H. Abé: Fracture Mechanics Applied to Hot, Dry Rock Geothermal Energy, in: Fracture Mechanics of Rock, (Ed. B. Atkinson), Academic Press, 1987, 241-276.

37. Ingraffea, A.R., K.L.Gaunsallus, J.F. Beech and P.P. Nelson: A Short Rod Based System for Fracture Toughness Testing of Rock, in: Chevron-Notched Specimens: Testing and Stress Analysis, ASTM STP 855, Louisville, (1983), 152-166.

38.Li, V. C., K. Chong, and H. H. Einstein, Tension Softening and Size Effects on Fracture Toughness Determination of Geomaterials, in: Fracture of Concrete and Rock, (Eds. Swartz and S. Shah), Springer-Verlag, New York, 255-264, 1989.

39. Li, V.C.: Mechanics of Shear Rupture Applied to Earthquake Zones, in Fracture Mechanics of Rock, (Ed. B.K. Atkinson), Academic Press, 1987, 351-432.

40. Bazant, Z.P., S. Sener and P.C. Prat: Fracture Mechanics Size Effect and Ultimate Load of Beams Under Torsion, in: Application of Fracture Mechanics to Concrete, Ed. V.C. Li and Z. Bazant, ACI STP, 1990, 171-178.

41. Wang, Y., V.C Li, and S. Backer: Tensile failure mechanisms in synthetic fiber reinforced mortar, submitted to the J. Materials Science (1990).

42. Li, V.C., Y. Wang, and S. Backer: A statistical-micromechanical model of tension-softening behavior of short fiber reinforced brittle matrix composites, submitted for publication, J. Mech. and Phys. of Solids (1990).

43. Li, V.C., Y. Wang, and S. Backer: Effect of inclining angle, bundling, and surface treatment on synthetic fiber pull-out from a cement matrix, to appear in Composites (1990).

44. Greszczuk, L. B.: Theoretical studies of the mechanics of the fiber-matrix interface in composites, in ASTM STP 452 (1969), 42-58.

45. Takaku, A. and R.G.C. Arridge: The effect of interfacial radial and shear stress on fiber pull-out in composite materials, Journal of Physics D: Applied Physics, 6 (1973), 2038-2047.

46. Lawrence, P.: Some theoretical considerations of fiber pull out from an elastic matrix, J. Mat.Sci.7, (1972) 1-6.

47. Gopalaratnam, V.S., and S.P. Shah: Tensile failure of steel fiber-reinforced mortar, ASCE J. of Engineering Mechanics, 113, 5, (1987), 635-652.

48. Wang, Y., V.C Li, and S. Backer: Modeling of fiber pull-out from a cement matrix, International J. of Cement Composites and lightweight Concrete, 10, 3, (1988), 143-149.

49. Wang, Y., V.C. Li, and S. Backer: Analysis of synthetic fiber pull-out from a cement matrix, Material Research Society Symposium Proceeding, 114, (1988), 159 -165.

50. Naaman, A., and S.P. Shah: Pull-out mechanism in steel fiber reinforced concrete, J. Struc., ASCE, 102, ST8, (1976), 1537-1548.

51. Wang, Y., V.C. Li, and S. Backer: Experimental determination of tensile behavior of fiber reinforced concrete, to appear in ACI Materials Journal (1990).

52. Wang, Y., V.C. Li, and S. Backer: Tensile properties of synthetic fiber reinforced mortar, to appear in J. of Cement Composites and Lightweight Concrete (1990).

53. Li, V.C., and E. Green: Tensile behavior of synthetic fiber reinforced high strength mortar and concrete, in preparation (1990).

54. Wang, Y., S. Backer, and V.C. Li: An experimental study of synthetic fiber reinforced cementitious composites, Journal of Materials Science, 22, (1987), 4281-4291.

55. Wang, Y., S. Backer, and V.C. Li: A special technique for determining the critical length of fiber pull-out from a cement matrix, J. of Materials Science Letters, 7 (1988), 842-844.

56. Li, V.C., Y. Wang and S. Backer: Effect of Fiber-Matrix Bond Strength on The Crack Resistance of Synthetic Fiber Reinforced Cementitious Composites, in: Bonding in Cementitious Composites (Eds. S. Mindess and S. Shah), MRS Symposia 114: 1988, 167-174.

57. Visalvanich K. and A.E. Naaman: In: Fracture Mechanics Methods for Ceramics, Rocks, and Concrete, ASTM STP 745, (Ed.S.W. Freiman and E.R. Fuller) 1981, 141-156.

58. Visalvanich, K. A.E. Naaman: Fracture Model for fiber reinforced concrete, ACI J. March-April, 1983, 128-138.

59. Petersson, P.E.: Crack Growth And Development Of Fracture Zone In Plain Concrete And Similar Materials. Div. of Building Materials, Lund Institute of Technology, Sweden. Report TVBM-1006, 1981.

60. Reinhardt, H.W.: Fracture Mechanics Of An Elastic Softening Material Like Concrete, Heron, Delft University of Technology, 29:2, 1984.

62. Marshall, D.B. and A.G. Evans: Failure mechanisms in ceramic-fiber/ceramic matrix composites, J. Am. Ceram. Soc., 68, 5 (1985) 225-31.

61. Gopalaratnam, V.S. and S.P. Shah,. Softening response of concrete in direct tension, J. Amer. Concrete Inst. 82:310 (1985).

63. Labuz, J.F., S.P. Shah and C. H. Dowding: Measurement and description of the tensile fracture process in rock, ASCE J. Eng. Mech., (1989).

64. Li, V.C.: Fracture Resistance Parameters For Cementitious Materials And Their Experimental Determination, in: Application of Fracture Mechanics to Cementitious Composites, (Ed. S.P. Shah) Martinus Nijhoff Publ., 1985, 431-452.

65. Li, V.C., C.M. Chan, and C.K.Y. Leung: Experimental determination of the tension softening relations for cementitious composites, Cement and Concrete Research, 17 (1987) 441-452.

66. Leung, C.K.Y. and V.C. Li: Determination of fracture toughness parameter of quasi-brittle materials with laboratory-size specimens, J. of Materials Science, 24, (1989) 854-862.

67. Li, V.C. and R. Ward: A Novel Testing Technique for Post-Peak Tensile Behavior of Cementitious Materials, in: Fracture Toughness and Fracture Energy -- Test Methods for Concrete and Rock, (Ed. Mihashi), in press, A.A.Balkema Publishers, Netherlands, 1989.

68. Chong, K.P., V.C. Li and H. Einstein: Size effects, process zone, and tension softening behavior in fracture of geomaterials", in press, Int'l J. of Engineering Fracture Mechanics, 1989.

69. Chong, K.P., K.D. Basham, and D.Q. Wang: Fracture parameters derived from tension-softening measurements using semi-circular specimens, in: Fracture Toughness and Fracture Energy -- Test Methods for Concrete and Rock, (Ed. Mihashi), in press, A.A.Balkema Publishers, Netherlands, 1989.

70. Hashida, T.: Tension-softening curve measurements for fracture toughness determination in granite, in: Fracture Toughness and Fracture Energy -- Test Methods for Concrete and Rock, (Ed. Mihashi), in press, A.A.Balkema Publishers, Netherlands, 1989.

71. Rice, J.R.: A path independent integral and the approximate analysis of strain concentrations by notches and cracks, J. Applied Mechanics, 35 (1968) 379-386.

72. Reyes, O.M.L.: Numerical Modelling Of Fracture Propagation In Tension Softening Materials, M.S. Thesis, MIT, Cambridge, MA, (1987).